Monthly Notices
of the
ROYAL ASTRONOMICAL SOCIETY

MNRAS **483,** 3168–3195 (2019)
Advance Access publication 2018 November 23

doi:10.1093/mnras/sty3075

Photometric redshifts for galaxies in the Spitzer Extragalactic Representative Volume Survey (SERVS)

Janine Pforr,[1]★† Mattia Vaccari [2,3] Mark Lacy [4] Claudia Maraston,[5] Kristina Nyland,[4] Lucia Marchetti [2,3,6] and Daniel Thomas [5]

[1]*Scientific Support Office, Directorate of Science and Robotic Exploration, European Space Research and Technology Centre (ESA/ESTEC), Keplerlaan 1, NL-2201 AZ Noordwijk, The Netherlands*
[2]*Department of Physics and Astronomy, University of the Western Cape, Robert Sobukwe Road, 7535 Bellville, Cape Town, South Africa*
[3]*INAF – Instituto di Radioastronomia, via Gobetti 101, I-40129 Bologna, Italy*
[4]*National Radio Astronomy Observatory, Charlottesville, VA 22903, USA*
[5]*Institute of Cosmology and Gravitation, University of Portsmouth, Dennis Sciama Building, Burnaby Road, Portsmouth PO1 3FX, UK*
[6]*Department of Astronomy, University of Cape Town, Private Bag X3, Rondebosch 7701, South Africa*

Accepted 2018 November 7. Received 2018 November 6; in original form 2018 January 15

ABSTRACT

We present photometric redshifts for ∼4 million galaxies detected in the *Spitzer* 3.6 or 4.5 μm bands of the Spitzer Extragalactic Representative Volume Survey (SERVS). The 18 deg^2 area of SERVS covers five extragalactic fields with a variety of ancillary, optical, and near-infrared (IR) photometry. We evaluate the accuracy of our photometric redshifts with ∼90.000 publicly available, spectroscopic redshifts. Overall, we find an average of ∼0.038 for the normalized median absolute deviation ($\sigma_{\rm NMAD}$), a measure similar to the standard deviation yet more robust against outliers, and *outlier fraction* η of 3.7 per cent for the sources with the widest wavelength coverage. On the example of the XMM field, we quantify the quality and reliability of photometric redshifts as a function of (1) the number of photometric bands available in the fitting, (2) $i_{\rm AB}$ magnitude, (3) Infrared Array Camera (IRAC) 3.6 μm magnitude, (4) spectroscopic redshift, and (5) the survey origin of the spectroscopic redshift. The best results are achieved when the photometry available for the fitting covers rest-frame optical and near-IR wavelengths. $\sigma_{\rm NMAD}$ and η are smallest for the brightest objects. Similarly, we find $\sigma_{\rm NMAD}$ and η to be smaller on average at $z < 1.5$ than at $z > 1.5$. Photometric redshifts derived without the two IRAC filter bands, but detections in all other bands are slightly underestimated. Approximately 76 per cent of SERVS sources with at least five available filter bands lie between redshift 0 and ∼1.5. We find a tail of high-redshift galaxies, i.e. ∼7 per cent of all objects with at least five available filter bands for the fitting lie at $z > 3$. We discuss ways to improve upon the photometric redshifts for SERVS galaxies in the future.

Key words: galaxies: distances and redshifts – galaxies: evolution – galaxies: formation – galaxies: fundamental parameters – galaxies: general .

1 INTRODUCTION

In the last decades, large galaxy surveys have driven galaxy evolution studies. Particularly, photometric data can be collected for large numbers of galaxies simultaneously. A few extragalactic fields are now prime targets for new surveys due to their already vast repertoire of photometric and spectroscopic data over large wavelength ranges which facilitate a true multiwavelength approach to studying galaxy evolution. The combination of photometry over a large wavelength range aids the estimation of basic galaxy parameters, such as stellar masses, star formation rates (SFRs) etc., using the popular approach of spectral energy distribution (SED) fitting of model galaxy templates to observed broad-band magnitudes. In the absence of spectroscopy, redshifts can also be derived photometrically using the SED-fitting approach (Baum 1962). Nowadays, there exist a multitude of publicly available codes to carry out this task to accommodate ever increasing object numbers, e.g. EAZY (Brammer et al. 2009), LEPHARE (Ilbert et al. 2006; Arnouts et al.

★ E-mail: janine.pforr@esa.int
† Research Fellow

1999), HYPERZ (Bolzonella, Miralles & Pelló 2000), to name just a few.

Since the onset of the era of large galaxy surveys, extensive studies have been carried out to test methods for the derivation of photometric redshifts (e.g. Bolzonella et al. 2000; Ilbert et al. 2009; Dahlen et al. 2013) and the stellar population properties of galaxies from SED fitting (Wuyts et al. 2009; Lee et al. 2009; Maraston et al. 2010; Pforr, Maraston & Tonini 2012, 2013; Mitchell et al. 2013; Mobasher et al. 2015). Using 30 medium filter bands in the Cosmic Evolution Survey (COSMOS, Scoville et al. 2007) field in the fitting Ilbert et al. (2009) achieved accuracies for photometric redshifts of $\sigma_{\Delta z/(1+z_{\rm spec})} = 0.007$ (where $\Delta z = z_{\rm spec} - z_{\rm phot}$) for galaxies brighter than $i^+_{\rm AB} < 22.5$ and $\sigma_{\Delta z/(1+z_{\rm spec})} = 0.012$ for galaxies at $i^+_{\rm AB} \sim 24$ and $z < 1.25$. Ilbert et al. (2013) improved upon their earlier results with the help of the new, deep UltraVISTA near-infrared (near-IR) data in the COSMOS field (McCracken et al. 2012) to $\sigma_{\Delta z/(1+z_{\rm spec})} = 0.03$ for galaxies between $1.5 < z < 4$, while typical photometric redshifts used for many galaxy evolution studies have accuracies in the range of $\sigma_{\Delta z/(1+z_{\rm spec})} \sim 0.02 - 0.04$ (see Ilbert et al. 2009, and references therein).

Several authors have compared photometric redshifts derived with different codes and methods (e.g. Hildebrandt et al. 2010; Dahlen et al. 2013). For example, Dahlen et al. (2013) studied several methods of determining photometric redshifts using broad-band multiwavelength photometry in the Cosmic Assembly Near-IR Deep Extragalactic Legacy Survey (CANDELS, Koekemoer et al. 2011; Grogin et al. 2011). While they found that different approaches in terms of photometric redshift code, SED templates, priors in the fitting lead to similar results in terms of photometric redshifts, they identified that outlier fractions and scatter are lowest when training samples of spectroscopic redshifts can be utilized. They found that the combination of results from multiple redshift codes and methods produces the smallest scatter and outlier fraction for the photometric redshifts.

In this paper, we determine and present photometric redshifts for galaxies in the Spitzer Extragalactic Representative Volume Survey (SERVS, Mauduit, Lacy & Farrah 2012), a *Spitzer Space Telescope* warm phase survey detecting ∼3.7 million objects in ∼18 deg^2 in five prominent, data-rich, extragalactic fields down to ∼2 μJy depth at 3.6 and 4.5 μm. SERVS is aimed at taking a complete census of the population of massive or IR-bright galaxies in the redshift range ∼1−6 within a volume of ∼0.8 Gpc^3, large enough to overcome the effects of cosmic variance that effect smaller fields, e.g. the Great Observatories Origins Deep Survey (GOODS, Dickinson, Giavalisco & GOODS Team 2003), the CANDELS Survey (Koekemoer et al. 2011; Grogin et al. 2011), and the COSMOS Survey (Scoville et al. 2007). The key goals of the survey address stellar mass assembly, obscured star formation, the role of active galactic nuclei (AGNs), the role of environment and the highest redshift quasars. Besides the key goals, the large area covered by SERVS enables studies of the large-scale structure at $z > 1$ as well as rare objects like massive, high-redshift galaxies and protoclusters, that are unlikely to be picked up by smaller surveys. All of these goals require accurate photometric redshifts in the absence of spectroscopic redshifts, which in turn will facilitate accurate and robust stellar masses and other galaxy property measurements as well as help in identifying the best samples for spectroscopic follow-up with current and future facilities such as the *James Webb Space Telescope*.

SERVS overlaps with many surveys at other wavelengths, e.g. the Visible and Infrared Survey Telescope for Astronomy (VISTA, Emerson et al. 2004) Deep Extragalactic Observations survey (VIDEO, Jarvis et al. 2013) in the near-IR, resulting in a wide variety of ancillary optical and near-IR photometry in addition to the Infrared Array Camera (IRAC) 3.6 and 4.5 μm imaging. While the wide wavelength coverage is ideal for SED fitting, the inhomogeneity of the optical and near-IR data across the SERVS fields provides a challenge. Unlike for smaller fields for which homogeneous data is available (e.g. COSMOS), each of the SERVS fields is comprised of different survey data in the bands bluewards of the *Spitzer* IRAC wavelengths and the multiwavelength coverage is inhomogeneous even in a single field.

For the SED fitting carried out in this paper, we therefore use multiband source catalogues from the SERVS data fusion project (see Section 2 of this work and Vaccari 2015). The SED-fitting method itself uses the HYPERZ code (Bolzonella et al. 2000). Given the large number of sources to fit within SERVS, we based our SED-fitting method on our earlier studies on how to accurately measure photometric redshifts while still using the most economic setup with respect to runtime and number of free parameters (Pforr et al. 2013). Details of this are laid out in Section 3. In Section 4, we present the derived photometric redshifts, and our quality assessments in terms of dependence on *i*-band magnitude, IRAC 3.6 μm magnitude (i.e. object brightness), spectroscopic redshift, and breadth of available photometry. The overall photometric redshift distribution of SERVS is presented in Section 5. We discuss aspects for improvement of the photometric redshifts such as source matching in Section 6. We finish with a comparison to other photometric redshift determinations in the literature in Section 7 and a summary in Section 8. Throughout this paper, we use a concordance cosmology with $H_0 = 71.9$, $\Omega_\Lambda = 0.742$, and $\Omega_{\rm Matter} = 0.258$ and AB magnitudes.

2 MULTIWAVELENGTH DATA

We make use of a wide range of multiwavelength data covering the observed-frame ultraviolet (UV) to the mid-IR which we will briefly describe in the following sections.

2.1 IR photometry from SERVS

The SERVS (PI: M. Lacy, Mauduit et al. 2012) was carried out during the warm phase of the *Spitzer Space Telescope*. Overall, five extragalactic fields, namely the Chandra Deep Field South (CDFS, Giacconi et al. 2001), The European Large Area *ISO* Survey (ELAIS, Oliver 1996; Oliver et al. 2000; Rowan-Robinson et al. 2004; Vaccari et al. 2005) N1 and S1 fields (hereafter EN1 and ES1, respectively), Lockman Hole (LH, Hasinger et al. 1993), and the centre of the *Spitzer* Wide-Area Infrared Extragalactic Survey (SWIRE, Lonsdale et al. 2003), XMM large-scale structure field (hereafter XMM) were observed at 3.6 and 4.5 μm (channels 1 and 2, respectively) with IRAC (Fazio et al. 1998, 2004) onboard the *Spitzer Space Telescope* down to ∼2 μJy (AB = 23.1 mag) depth. Together, these fields cover an area of 18 deg^2 with the aim to mitigate cosmic variance. A brief overview of the SERVS fields in terms of location, field size, and number of detected sources can be found in Table 1. These fields were chosen to complement the existing optical and near-IR data described in the next section.

The survey itself, its comparison to other IR surveys, as well as details on the source detection and extraction for data release 1 (DR1) in SERVS is described in Mauduit et al. (2012). Briefly, sources were extracted using SOURCE EXTRACTOR(Bertin & Arnouts 1996), and fluxes computed for several aperture radii. Aperture fluxes were aperture corrected and calibrated using SWIRE (Lonsdale et al. 2003) data for sources common to both surveys. In this work, we

Table 1. Summary of the five SERVS fields. We only list the number of sources with spectroscopic redshifts for those objects which are not near bright stars in either of the two IRAC bands, have at least CSNR≥3 in both IRAC bands, and with the restrictions applied to the spectroscopic catalogues listed in Section 2.3, since these are the sources we compare our photometric redshifts to in Section 4.

SERVS field	RA (J2000)	Dec. (J2000)	Field size	Number of sources	Number of sources with $z_{\rm spec}$
CDFS	03:32:19	−28:06	4.5 deg^2	829191 (22.2 per cent)	20890 (0.56 per cent)
EN1	16:10:00	+ 54:30	2.0 deg^2	395179 (10.6 per cent)	1582 (0.04 per cent)
ES1	00:37:48	−44:00	3.0 deg^2	605932 (16.2 per cent)	7496 (0.20 per cent)
LH	10:49:12	+ 58:07	4.0 deg^2	951102 (25.4 per cent)	3512 (0.09 per cent)
XMM	02:20:00	−04:48	4.5 deg^2	958421 (25.6 per cent)	41632 (1.11 per cent)
Total	-	-	18 deg^2	3739825	75212 (2.01 per cent)

Table 2. Overview of the number of objects in each SERVS field with a CSNR as defined in Mauduit et al. (2012) larger than 0 at 3.6 μm, larger than 0 at 4.5 μm, and ≥3 at 3.6 μm and at 4.5 μm. Note that CSNR$_x$ ≤ 0 not only indicates non-detections in band x, but also objects not observed in that band due to lack of areal coverage compared to the other IRAC band.

SERVS field	Number of sources with		
	CSNR$_{3.6\,\mu{\rm m}} > 0$	CSNR$_{4.5\,\mu{\rm m}} > 0$	CSNR$_{3.6+4.5\,\mu{\rm m}} \geq 3$
CDFS	618735	630921	398183
EN1	292717	298645	187509
ES1	447874	454787	281829
LH	682269	721220	437733
XMM	707763	727317	452598

use the aperture corrected 1.9 arcsec aperture fluxes in the IRAC 3.6 and 4.5 μm bands from SERVS data release 2 (DR2) as contained in the SERVS data fusion (see also Table 3). SERVS DR2 (Vaccari 2015, http://www.mattiavaccari.net/df) is a superset of SERVS DR1 (Mauduit et al. 2012), which was cut at S/N = 10, and therefore DR2 contains twice as many sources as DR1. Since we expect IRAC to be a powerful photometric redshift constraint in its own right and the identification of high-redshift sources is highly desired, we use DR2 and provide photometric redshift estimates also for sources with relatively low signal-to-noise ratio (S/N).

While SERVS DR2 is not strictly S/N-selected, the vast majority of sources in DR2 has a coverage-weighted S/N (CSNR) as defined in Mauduit et al. (2012) larger than 3 in at least one of the two IRAC bands as shown in Fig. 1. While we attempt to compute photometric redshifts for all sources in the DR2 catalogues as pointed out earlier, we will restrict our comparison with spectroscopic redshifts to objects with CSNR ≥3 in both IRAC bands. Table 2 provides a quick overview of the number of objects above and below this threshold. Note however, that the overlap between the images in the IRAC 3.6 and 4.5 μm bands is not perfect. Consequently, a CSNR$_x$ ≤ 0 not only indicates non-detections in band x but also objects not observed in that band compared to the other IRAC band. Additionally, we exclude any object whose mask flag indicates the presence of a bright star (mask flag ≥512, see table 4 in Mauduit et al. 2012) from our photometric redshift performance estimates.

2.2 SERVS data fusion – optical and near-IR photometry

The SERVS data fusion,[1] i.e. the cross-match of SERVS sources to other multiwavelength data, was carried out by Vaccari (2015). It is based on the SERVS IRAC 3.6 and 4.5 μm band-merged and cross-matched catalogues which is described in detail in Mauduit et al. (2012) but provides deeper IRAC 3.6 and 4.5 μm catalogues compared to Mauduit et al. (2012) as pointed out in the previous section. The SERVS data in each field are then cross-matched to existing multiwavelength catalogues from a variety of external surveys, ranging from the observed-frame UV to the far-IR, applying a 1 arcsec search radius around any given SERVS–IRAC source. In general, the data fusion was carried out following the recommendations of the respective ancillary catalogues with respect to masked regions. A summary of the existing multiwavelength data used in this paper is listed in Table 3 (for details on the full set of multiwavelength data available, see Vaccari 2015). A more comprehensive overview of the ancillary optical and ground-based near-IR surveys with survey depths is also given in Mauduit et al. (2012) and Chen et al. (2018) as well as Table 3.

We provide an overview over the number of sources with rich multiwavelength data in the selected ancillary surveys in Fig. 2. The large number of objects with only one or two filters available stems from the large number of SERVS sources, detected at either 3.6 or 4.5 μm, or both, that do not have cross-matches with any of the ancillary data catalogues, partly due to a lack of overlap in areal coverage and survey depth. This drastically reduces the number of sources for which photometric redshifts can be determined reliably with the given data set (e.g. Bolzonella et al. 2000; Pforr et al. 2013). For each field between 10 and 12 filter bands are available in total, though not all sources are observed by all ancillary surveys or detected in each band due to survey depth and/or lack of areal coverage. We discuss on how to improve on the inhomogeneity of the ancillary data and consequently the photometric redshifts in Section 6.

2.2.1 Inhomogeneity of survey depths and sizes, and corrections

The available multiwavelength data are inhomogeneous across the SERVS fields in terms of areal coverage and depth. We note that small portions of the five SERVS fields have very deep photometry from other surveys (e.g. GOODS-S) with which robuster photometric redshifts for individual sources could be achieved. However, given the large number of sources in each SERVS field (see Ta-

[1] www.mattiavaccari.net/df

Table 3. Multiwavelength measurements contributing to the SERVS data fusion that were used in the SED fitting in this paper along with sizes of aperture radii and survey depths as reported in the literature. All aperture magnitudes are aperture corrected. A compilation of filter curves employed in the fitting and provided by M. Vaccari can be found at http://mattiavaccari.net/df/filters/ [i].

Field	Optical	Near-IR	IR	Max filter number
CDFS	CTIO[a]	VHS/VIDEO[f]	SERVS[h]	12
	ugriz	*ZYJHKs*	IRAC 3.6 μm, 4.5 μm	
	1.6 arcsec	2 arcsec	1.9 arcsec	
	m_{AB} ∼26 (*ugri*, co-added, multi-epoch)	*ZYJHKs* to m_{AB} ∼23.8-25.7	2 μJy, e.g. CSNR = 10 (DR1)	
EN1	INT–WFC [b]	UKIDSS–DXS[g]	SERVS[h]	10
	ugriz	*JHK*	IRAC 3.6 μm, 4.5 μm	
	1.7 arcsec	2 arcsec	1.9 arcsec	
	23.9, 24.5, 24.0, 23.3, 22.0 (*ugriz*, AB, 5σ)	$J \sim 23.2$, $K \sim 22.7$ (AB, 5σ)	2 μJy, e.g. CSNR = 10 (DR1)	
ES1	WFI + VIMOS[c]	VHS/VIDEO[f]	SERVS[h]	12
	BVR + *Iz*[c]	*ZYJHKs*	IRAC 3.6 μm, 4.5 μm	
	2 arcsec for *BVR* and 1.64 arcsec for *Iz*	2 arcsec	1.9 arcsec	
	m_{AB} ∼26 (VOICE data products)	*ZYJHKs* to m_{AB} ∼23.8–25.7	2 μJy, e.g. CSNR = 10 (DR1)	
	m_{Vega} ∼23.1, 22.5 (*Iz*, 90 per cent completeness)			
LH	INT–WFC + KPNO[d]	UKIDSS–DXS[g]	SERVS[h]	10
	ugriz	*JHK*	IRAC 3.6 μm, 4.5 μm	
	1.7 arcsec	2 arcsec	1.9 arcsec	
	23.9, 24.5, 24.0, 23.3, 22.0 (*ugriz*, AB, 5σ)	$J \sim 23.2$, $K \sim 22.7$ (AB, 5σ)	2 μJy, e.g. CSNR = 10 (DR1)	
XMM	CFHTLS-W1[e]	VHS/VIKING/VIDEO[f]	SERVS[h]	12
	ugri(*y*)*z*	*ZYJHKs*	IRAC 3.6 μm, 4.5 μm	
	MAG_AUTO	2.0 arcsec	1.9 arcsec	
	$m_{AB} \sim 24.5$ in *i'*	*ZYJHKs* to m_{AB}∼23.8-25.7	2 μJy, e.g. CSNR = 10 (DR1)	

Notes: [a] Cerro Tololo Inter-American Observatory (CTIO)-MOSAIC2-*Ugriz* optical imaging catalogs by Siana (private communication) [Vega]. The photometry will be released together with the VST Optical Imaging of the CDFS and ES1 Fields (VOICE) data products (Vaccari et al. 2016).
[b] Isaac Newton Telescope–Wide field camera (INT–WFC) *ugriz* optical imaging catalogues by González-Solares et al. (2011) [AB].
[c] Wide field Imager (WFI)–*BVR* and VIMOS *I* and *z* optical imaging catalogues by Berta et al. (2006, 2008) [Vega], and re-reduced by Vaccari et al. (2016). See the text for a description of the aperture correction in ES1 *I, z* filter bands.
[d] INT–WFC + Kitt Peak National Observatory (KPNO) MOSAIC1 'Merged' optical imaging catalogues by González-Solares et al. (2011). The KPNO data reduction was carried out exactly as for the INT–WFC data. The INT and KPNO filters were judged to be similar enough to combine the two catalogues by applying a small colour correction to the KPNO magnitudes and putting everything on the INT flux scale [AB].
[e] Canada–France–Hawai'i Telescope Legacy Survey Wide Field 1 (CFHTLS-W1) *ugriz* optical imaging catalogues from CFHTLS T0005 DR (www.cfht.hawaii.edu/Science/CFHTLS) [AB]
[f] VIDEO DR3/VISTA Kilo-Degree Infrared Galaxy Survey (VIKING, Edge et al. 2013), DR3/VISTA Hemisphere Survey (VHS, McMahon et al. 2013), DR2 from VISTA Science Archive (Jarvis et al. 2013) [Vega].
[g] UKIDSS DXS (Lawrence et al. 2007) [Vega], for survey depths see also (Kim et al. 2014).
[h] Mauduit et al. (2012); Vaccari (2015).
[i] The filter response curves that we employed in the fitting from this compilation are the following (listed as 'Filter - Number in compilation'): INT WFC u–0225, INT WFC g–0226, INT WFC r–0227, INT WFC i–0228, INT WFC z–0229, United Kingdom Infrared Telescope (UKIRT) WFCAM (UKIDSS) J–0222, UKIRT WFCAM (UKIDSS) H–0223, UKIRT WFCAM (UKIDSS) K–0224, WFI B–0163, WFI V–0158, WFI Rc–0159, VIMOS I–0266, VIMOS z–0267, VISTA VIRCAM Z–0362, VISTA VIRCAM Y–0363, VISTA VIRCAM J–0364, VISTA VIRCAM H–0365, VISTA VIRCAM Ks–0366, CTIO U–0240, CTIO g–0236, CTIO r–0237, CTIO i–0238, CTIO z–0239, IRAC1–0198, IRAC2–0199

ble 1) for which photometric redshifts need to be determined we focus in this work on the most homogeneous data by balancing width and depth of the ancillary surveys in one particular field. We point out however, that between the different SERVS fields, photometry will still be inhomogeneous in depth and coverage since no single survey besides SERVS covers all five fields. We utilize aperture magnitudes wherever possible and choose apertures as close to each other as possible across the different wavelength ranges. Most aperture magnitudes provided in the data fusion catalogues are aperture corrected. The exception are the *I z* filters in ES1 for which no aperture correction was applied in the initial data fusion catalogues. For these, we derived an aperture correction by computing the difference between auto magnitudes and aperture magnitudes for a 1.64 arcsec aperture radius (MAG_AUTO-MAG_APER) for each object and then determining the peak of the distribution for each band. We then corrected the aperture magnitudes in *I* band with a −0.0075 mag offset as determined by this method, and those in *z* band with −0.0135 mag.

If no aperture magnitudes are provided we use MAG_AUTO, which is the case for the optical magnitudes in the XMM field. Given that MAG_AUTO represents a total magnitude similarly to aperture corrected aperture magnitudes and that the offsets we found for ES1 were much smaller than the average photometric errors in these bands, this should not affect the fits in a strong way for most sources. The exact magnitude types and apertures used for each data set are listed in Table 3.

The heterogeneity of the data sets is such that a homogeneous measure of the depths of the different catalogues we used is difficult to obtain. We list the values gathered from the respective publications cited in Table 3 for these surveys, though point out that these are not computed or reported homogeneously. For an overview on survey depths in XMM, CDFS, and ES1 across a broader wave-

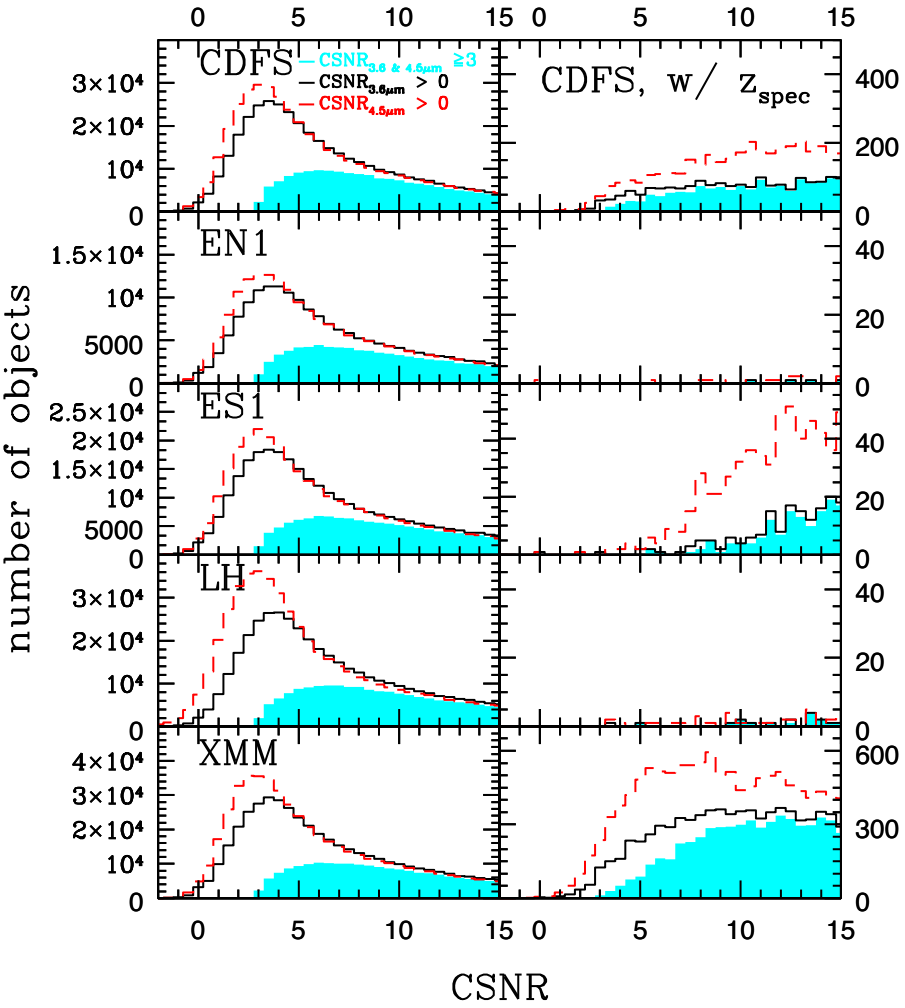

Figure 1. Number of objects as a function of CSNR in the five SERVS fields. The black empty histograms show all objects in the respective fields with CSNR >0 in the 3.6 μm band, the empty red dashed line histograms show all objects in the respective fields with CSNR >0 in the 4.5 μm band, and the cyan filled histograms show all objects for which CSNR≥3 in the 3.6 and 4.5 μm band. The left-hand panels show the same histograms for sources for which also a spectroscopic redshift is available. The total number of spectroscopic redshifts in the EN1 and LH fields is sparse compared to the other fields (see also Table 1). Note that the scale showing the number of objects changes from panel to panel. Objects flagged as being in close proximity to a bright star in either of the two IRAC bands were excluded.

length range and including surveys not used in this work, we refer the reader also to Chen et al. (2018). Lastly, we point out that the Herschel Extragalactic Legacy Project team is undertaking homogenization of data over a wider wavelength range (Vaccari 2016).

The typical seeing for the optical and near-IR data is between 0.8 and 1.2 arcsec. This is significantly better than the seeing for SERVS in the warm phase of the *Spitzer Space Telescope* which is ∼2 arcsec.[2]

Not all magnitudes are given in the AB system in the original catalogues. For those in the Vega system, we use the following correction x for the filter i applied as $m_{\rm AB} = m_{\rm Vega} + x_i$. The corrections are listed in Table 4. SERVS AB magnitudes are directly calculated from the fluxes given in μJy with $m_{\rm AB} = -2.5 \times \log_{10}(\mathrm{flux}[\mu Jy]) + 23.9$.

[2]https://irsa.ipac.caltech.edu/data/SPITZER/docs/irac/iracinstrumenthandbook/5/

2.3 Spectroscopic redshifts

The SERVS fields profit from a large amount of publicly available spectroscopic data. In Table 5, we list the spectroscopic redshift catalogues to which we compare our derived photometric redshifts in order to assess reliability and accuracy of the latter. The spectroscopic catalogues have been cross-matched within a search radius of 0.5 arcsec and cleaned to contain only reliable redshifts as much as possible taking into account the redshift flag information given by the various surveys (http://www.mattiavaccari.net/df/specz/, Vaccari 2015). Additionally, we applied the following selections:

(i) For redshifts from the Visible Multi-Object Spectrograph (VIMOS) Very Large Telescope (VLT) Deep Survey [VIMOS-VLT Deep Survey (VVDS), Le Fèvre et al. 2013] used for XMM and CDFS we only compare to spectroscopic redshifts with flags 3 and 4 (and 13 and 14 for AGN, as well as 23 and 24 for secondary targets, etc.), which are listed with confidence levels of 95 and 100 per cent, respectively.

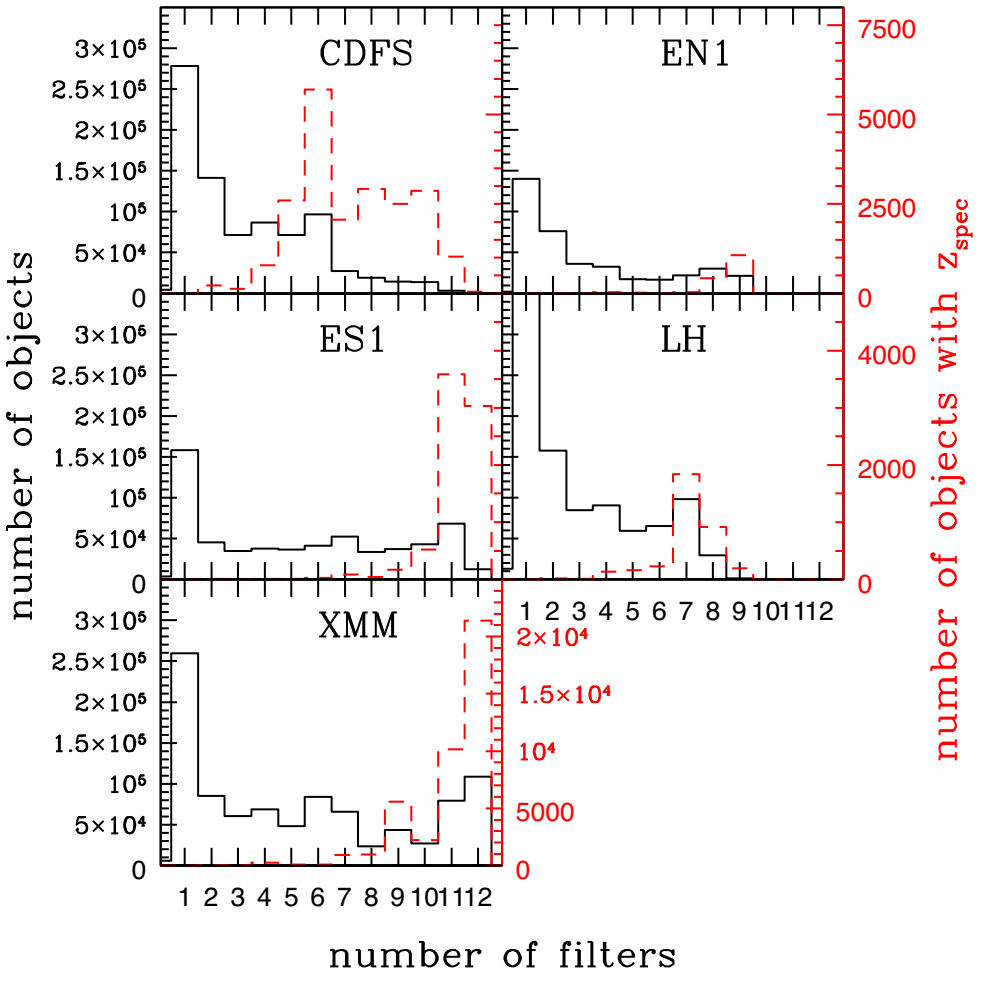

Figure 2. Number of objects as a function of available number of filters for the SED fitting in all five SERVS fields. The black empty histograms show all objects in the respective catalogues, the empty red, dashed line histograms only show the distribution of sources with available spectroscopic redshifts after mask flags, CSNR, and the limits listed in Section 2.3 were applied. Note that the scale showing the number of objects is different for the black and red histograms and also differs in each row. The maximum filter number in LH and EN1 is 10, and 12 in the other fields.

(ii) For BLAST−SPECZ (Eales et al. 2009; Moncelsi et al. 2011), we only included Q_OP>3 sources. Q_OP is adopted from RUNZ with quality 5 defined as definite redshift and quality 4 refers to ∼95 per cent confidence.

(iii) For ACES, we only included ZQUALITY>2 which denotes a reliability of $\gtrsim$ 90 per cent and the existence of multiple spectral features.

(iv) From the ECDFS−GOODS−CANDELS November 2014 release by Hsu et al. (2014), we only included redshifts with qualities of 0 and 1 which indicate high, and good spectroscopic redshift quality, respectively.

(v) For the PRIsm MUlti-Object Survey (PRIMUS) DR1 (Coil et al. 2011; Cool et al. 2013), we only included sources which satisfied ZQUALITY≥3, i.e. those with $\Delta z/(1+z) \lesssim 0.015$, and TARGET_MAG <23.0.

(vi) For the VIMOS Public Extragalactic Redshift Survey (VIPERS) PDR2 (Guzzo & The Vipers Team 2013; Garilli et al. 2014; Scodeggio et al. 2018) covering the XMM field we kept only objects with spectroscopic redshift flags between 3 and 4.5 (and between 13 and 14.5 for AGN, as well as between 23 and 24.5 for secondary targets). Flags 3 and 4 in this catalogue indicate ∼99 per cent secure spectroscopic redshifts, based on clear spectral features, with low and high S/N spectrum for flags 3 and 4, respectively. The decimal point indicates the level of agreement between spectroscopic and photometric redshifts; however, photometric redshifts were not used to determine the spectroscopic redshift.

(vii) For UDSz (spectroscopic follow-up of the UKIDSS Ultra-Deep Survey, 140325 release, Bradshaw et al. 2013; McLure et al. 2013) used for XMM, we kept spectroscopic redshifts with flags 3 and 4 if they stem from VIMOS and flags A and B if they stem from FOcal Reducer/low dispersion Spectrograph 2 (FORS2) for which flags 4 and A correspond to the most secure redshifts with multiple spectral features and flags 3 and B are considered very reliable based on cross-correlation and visual classification.

(viii) For the CfA HectoSpec Spitzer Follow-up spectroscopic redshifts used for LH, we restricted ourselves to flags 3 and 4 which are deemed reliable.

(ix) For SDSS DR14 (Abolfathi et al. 2018), we only used sources with ZWARNING =0, i.e. those sources without known problems.

Spectroscopic redshift catalogues listed in Table 5 for which no selections are listed above were used as provided by the teams and publicly available without further restrictions.

Table 4. Corrections to convert from Vega to AB magnitudes that were used in this work. The correction x for the filter i is applied as $m_{\rm AB} = m_{\rm Vega} + x_i$.

Filter	Correction	Reference
CTIO *U*	0.728	Vaccari (2015); Vaccari et al. (2016)
CTIO *g*	−0.096	Vaccari (2015); Vaccari et al. (2016)
CTIO *r*	0.159	Vaccari (2015); Vaccari et al. (2016)
CTIO *i*	0.392	Vaccari (2015); Vaccari et al. (2016)
CTIO *z*	0.552	Vaccari (2015); Vaccari et al. (2016)
WFI *B*	−0.0999	Vaccari (2015)
WFI *V*	−0.0055	Vaccari (2015)
WFI *R*	0.2048	Vaccari (2015)
VIMOS *I*	0.456	Vaccari (2015)
VIMOS *z*	0.5624	Vaccari (2015)
UKIDSS *J*	0.938	Hewett et al. (2006)
UKIDSS *H*	1.379	Hewett et al. (2006)
UKIDSS *K*	1.9	Hewett et al. (2006)
VISTA *Z*	0.521	González-Fernández et al. (2018) /VISTA webpages[a]
VISTA *Y*	0.618	González-Fernández et al. (2018) /VISTA webpages
VISTA *J*	0.937	González-Fernández et al. (2018) /VISTA webpages
VISTA *H*	1.384	González-Fernández et al. (2018) /VISTA webpages
VISTA K_s	1.839	González-Fernández et al. (2018) /VISTA webpages

Notes: [a]We used and listed the VISTA pipeline version 1.3 values as detailed on the VISTA webpages: http://casu.ast.cam.ac.uk/surveys-projects/vista/technical/filter-set. The updated values in González-Fernández et al. (2018) differ from the v1.3 values by less than the minimum photometric error that we apply in the fitting.

Since a single object can have more than one spectroscopic redshift from different sources, we defined a ZBEST parameter for the spectroscopic redshifts which we then use in the statistical comparisons and figures unless stated otherwise. To first order ZBEST is simply ordered by catalogue. The catalogue order is indicated in Table 5 for each field. If catalogue 1 contains a spectroscopic redshift, this redshift will be used as ZBEST. If the first catalogue does not contain a spectroscopic redshift for the source, the entry in the second catalogue is tested. A positive result for this check means this $z_{\rm spec}$ is used as ZBEST; a negative result leads to testing the spectroscopic redshift in the third catalogue. This chain is continued until the last catalogue is reached. However, this simple procedure does not account for multiple spectroscopic redshifts from different sources for a single object. In case of multiple $z_{\rm spec}$ entries, we keep the object and the above $z_{\rm spec}$ order if the redshifts agree with each other within $|\Delta z_{\rm spec}| < 0.01$ corresponding to the basic redshift step resolution we test for in the photo-z fitting described in Section 3. Objects with multiple $z_{\rm spec}$ entries that differ more than this from each other are discarded for the merged results (i.e. no ZBEST is chosen) and only taken into account in the catalogue by catalogue figures and statistics. We illustrate the distribution of objects with reliable (as defined by the above flags for each survey and merging to ZBEST) spectroscopic redshifts and CSNR≥3 in both IRAC bands not flagged as located near bright stars as a function of number of filters available for the SED fitting in Fig. 2 in red. CDFS and XMM are the fields with the most spectroscopic redshifts. Particularly, for XMM, the number of objects that also have broad-band photometry across the UV to IR wavelength range provide the best subset to test our photometric redshifts. While CDFS would also be a useful test case, the quality of the existing optical data is not on a par with XMM−LSS, and the photometric redshift performance would arguably be driven by that. We reserve to compute improved photometric redshifts in CDFS making use of the VLT Survey Telescope (VST) Optical Imaging of the CDFS and ES1 Fields (VOICE) optical data set (Vaccari et al. 2016) when it becomes fully available. Therefore, in the following, we will focus on XMM to demonstrate our case in detail, while providing basic information about the quality of the photometric redshifts in the other fields. We show the distribution of the sources in XMM described by their IRAC 3.6 μm magnitude as a function of the spectroscopic redshift in Fig. 3. Due to the lack of sources with spectroscopic redshifts larger than ∼1.5, we find fewer galaxies between redshift 1.5 and ∼5 and most sources lie at lower redshift.

3 PHOTOMETRIC REDSHIFTS

Photometric redshifts were obtained through SED fitting using HYPERZ (Bolzonella et al. 2000) with a variety of templates and a Calzetti et al. (2000) reddening law. HYPERZ finds the best-fitting template through χ^2 minimization comparing galaxy template spectra (model SEDs of stellar populations) to the observed data. χ^2 is calculated as:

$$\chi^2 = \sum_{i=1}^{N} \left[\frac{F_{\rm obs,i} - b \times F_{\rm temp,i}}{\sigma_{\rm i}^2} \right]^2,$$

where $F_{\rm obs,\,i}$ and $F_{\rm temp,\,i}$ are the observed and template fluxes in filter band i, $\sigma_{\rm i}$ is the photometric error, N is the number of filter bands, and b is the normalization. HYPERZ provides the photometric redshift, the best-fitting template spectrum and the reduced χ^2 ($\chi^2_{\rm r}$) for each observed object. The only fitted parameter is then the normalization b between template and observed fluxes (as described in the HYPERZ manual and also section 4 of Salim et al. 2007, in which b is labelled as scale factor a). As Salim et al. (2007) stress, the normalization should not be confused with the galaxy parameters in each template spectrum. Consequently, the degrees of freedom in the fit − given by the number N of photometric filter bands available in the fit − to determine the $\chi^2_{\rm r}$ are then reduced by one and $\chi^2_{\rm r}$ is calculated as $\chi^2/(N-1)$ within HYPERZ (Bolzonella et al. 2000). We refer the reader to Bolzonella et al. (2000) and Salim et al. (2007) for a full description of this formalism.

We adopt the template setup that was determined to provide the best balance in terms of CPU runtime and photometric redshift success by Pforr et al. (2013) which is based on the Maraston (2005) stellar population models. It consists of 16 theoretical spectra with exponentially declining star formation histories, so-called τ-models where τ denotes the e-folding time and assumes values of 0.1, 0.3, 1, and 2 Gyr, and metallicities of $\frac{1}{5}$, $\frac{1}{2}$, 1, and 2 $Z_\odot$. A Salpeter (1955) initial mass function is assumed for all templates. We keep the original age grid of 221 ages equivalent to the age grid of standard Bruzual & Charlot (2003) templates but restrict the minimum age to 0.1 Gyr and the maximum age to the age of the Universe at the probed redshift. We restrict absolute magnitudes in the UKIRT Infrared Deep Sky Survey (UKIDSS) K band to lie between −12 and −30 mag for all fits to exclude unreasonable solutions. It is worth noting that only a handful of objects in each SERVS field receive a best-fitting solution for which the absolute K-band magnitude equals these limits (26 in CDFS, 33 in EN1, 50 in ES1, 35 in LH, and 51 in XMM). Specifically, in the cases of absolute K magnitudes of −12 mag, the derived photometric redshifts are extremely low, i.e. $z_{\rm phot} < 0.05$ and these objects are likely stars. In the cases of absolute

Table 5. Overview of the spectroscopic catalogues compiled by Vaccari (2015, see also http://www.mattiavaccari.net/df/specz/) and used in this work for the comparison to the photometric redshifts. The numbers indicate the order in each field in which the spectroscopic catalogues were probed for the ZBEST.

Survey origin of spectroscopic redshift	CDFS	EN1	ES1	LH	XMM
VVDS−CDFS−DEEP (Le Fèvre et al. 2013)	1				
BLAST−SPECZ (Eales et al. 2009; Moncelsi et al. 2011)	2				
ACES 111127 release(Cooper et al. 2012)	3				
Mao et al. (2012)	4		2		
PRIMUS-DR1 (Coil et al. 2011; Cool et al. 2013)	5		3		4
ECDFS−GOODS−CANDELS November 2014 release (Hsu et al. 2014)	6				
OzDES-DR1 (Yuan et al. 2015; Childress et al. 2017)	7		4		8
VUDS-DR1 (Le Fèvre et al. 2015; Tasca et al. 2017)	8				
Trichas et al. (2009)		1			
ITP 2010 HerMES Follow-Up (Perez-Fournon, private communication)		2		4	
SDSS-DR14 (Abolfathi et al. 2018)		3		5	7
Sacchi et al. (2009)			1		
CfA HectoSpec Spitzer Follow-Up (Rigopoulou, private communication)				1	
Owen & Morrison (2009)				2	
ICL WHT SWIRE Follow-Up (Patel et al. 2011)				3	3
VVDS-02HR-DEEP-UDEEP (Le Fèvre et al. 2013)					1
UDS compilation 101018 release (Smail et al. 2008; Simpson et al. 2012)					2
VIPERS-PDR2 (Guzzo & The Vipers Team 2013; Garilli et al. 2014; Scodeggio et al. 2018)					5
UDSz 140325 release (Bradshaw et al. 2013; McLure et al. 2013)					6
GAMA DR3 (Liske et al. 2015; Baldry et al. 2018)					9

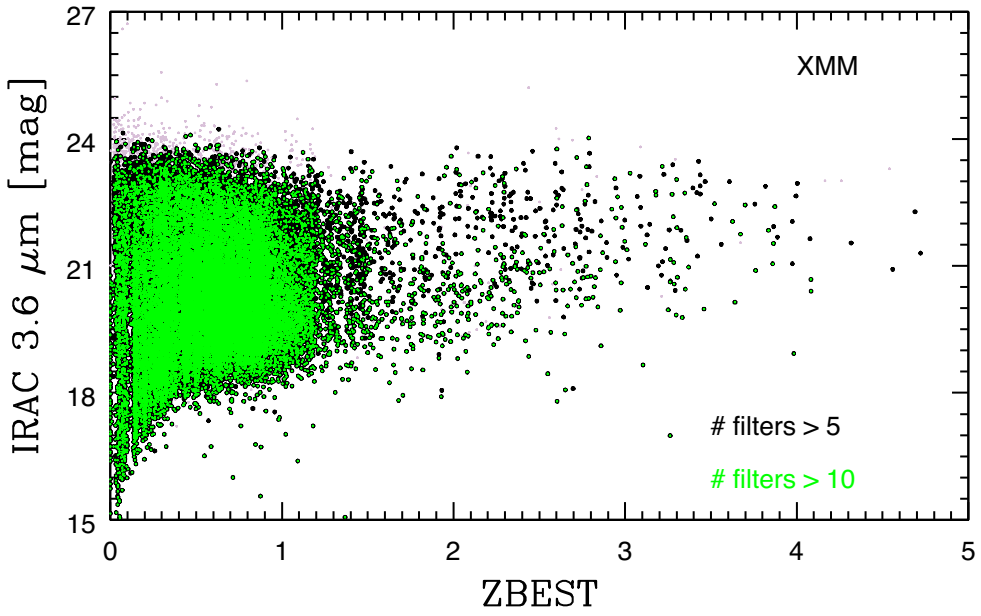

Figure 3. Objects in XMM with available spectroscopic redshift (ZBEST, as described in the text) versus their IRAC 3.6 μm magnitude. The black dots show all objects with more than five filter bands, while the green dots show only those with more than 10 filter bands available in the fitting. A CSNR≥3 cut was applied for both IRAC bands, as well as the restrictions to the various spectroscopic redshifts explained in the main text. The faint grey points show objects below the CSNR cut in either of the two IRAC bands.

K magnitudes of −30 mag, the derived photometric redshifts are higher, but the fits are very bad, typically with $\chi^2_r > 10$. We vary the redshift from 0 to 6 in steps of 0.01. In comparison to Pforr et al. (2013), we use this refined redshift grid – redshift steps of 0.01 instead of 0.05 – for the SERVS photometric redshifts in order to better enable environmental studies in SERVS. The reddening A_V was varied from 0 to 3 in steps of 0.2. The best photometric redshift is then determined by the template and parameter combination that provides the smallest χ^2_r.

Note that our template set does not contain any star or AGN templates. Consequently, results for these types of objects will be misleading. For AGN, the derived photometric redshifts will only be affected if the AGN contributes significantly to the light emission in the rest-frame UV to near-IR. We discuss this further in Section 6.3.

3.1 Probability distribution functions

HYPERZ contains the option to retrieve matrix files containing all solutions with their χ^2_r within the tested parameter space. However, these files are extremely large (e.g. 63 MB per object for the 0.05 redshift binning and even larger in our setup) and thus quickly exceed available disk space when dealing with large surveys such as SERVS. Therefore, we modified the HYPERZ routine with permission from M. Bolzonella to internally sum the probabilities at each redshift step and for each template and output the PDF(z)s (probability distribution functions) for each template within the same file instead of the matrix files $*.m$. We designate these new output files with $*.p$. The $*.p$ files have the following format:

z, P(z, template$_1$*), P(z,* template$_2$*), ..., P(z,* template$_n$*)*

for n templates being used in the fitting. In our case $n = 16$. The full PDF(z) is then simply obtained by the following sum: PDF(z)=Σ P(z, template$_i$) for each redshift bin. This results in an 'unnormalized' PDF(z). A simple normalization can be included by normalizing the probability at each redshift with the total probability in the full PDF(z). The resulting $*.p$ files then only have a size of 24 KB for the $\Delta z = 0.05$ grid and 128 KB for the $\Delta z = 0.01$ grid, which is a much more manageable amount of data for a large survey such as SERVS.

The PDF(z)s are available upon request. The photometric redshifts will be made available through CDS/Vizier. Some examples for best-fitting solutions and the according PDF(z) for objects with a spectroscopic redshift from the VVDS Survey in XMM chosen for their spread in redshift, and goodness of fits (expressed as χ^2_r), are presented in Figure 4-6. Despite some seemingly bad fits in terms of χ^2_r, the PDF(z)s for these objects are mostly single peaked because the larger number of available filter bands in the fit is sufficient to exclude other redshift solutions.

4 QUALITY OF PHOTOMETRIC REDSHIFTS

We present our derived photometric redshifts in comparison to the available spectroscopic redshifts predominantly for XMM as our example field. We chose XMM, since this is the field with the largest number of spectroscopic redshifts available for comparison. In order to assess the quality of our photometric redshifts in comparison to spectroscopic redshifts, we use the following statistics, which are commonly used to describe photometric redshift quality (e.g. see Ilbert et al. 2006; Brammer et al. 2009; Dahlen et al. 2013):

$$\sigma_{\rm NMAD} = 1.48 \times {\rm median}[|\frac{(\Delta z - {\rm median}(\Delta z))}{(1 + z_{\rm spec})}|]$$

where

$$\Delta z = z_{\rm spec} - z_{\rm phot}.$$

The normalized median absolute deviation $\sigma_{\rm NMAD}$ (Huber 1981; Hoaglin, Mosteller & Tukey 1983) is often used in photometric redshift studies (e.g. Brammer et al. 2009) and is equal to the standard deviation for a Gaussian distribution but less sensitive to outliers than just the difference between photometric and spectroscopic redshifts (Ilbert et al. 2006). We use the common definition of catastrophic outliers

$$|\Delta z| > 0.15 \times (1 + z_{\rm spec})$$

(e.g. Ilbert et al. 2006, 2009; Dahlen et al. 2013) and in the following refer to the *outlier fraction* as η. We further calculate the *median*, *mean* $\pm 1\sigma$ and *rms* for

$$\frac{\Delta z}{(1 + z_{\rm spec})}.$$

We restrict our sample to sources with ZBEST>0. In the following sections, we will assess the quality of our photometric redshifts in different scenarios.

4.1 Dependence on number of filter bands

We will investigate the dependence of the quality of photometric redshifts on the number of filter bands in the next sections in two ways; first, separate for each of the SERVS fields, and second, for each spectroscopic source catalogue for the XMM field as an example.

4.1.1 Distinction by extragalactic field

In order to provide a brief overview of the difference in photometric redshift quality for the different SERVS fields, we plot the *rms*, *median*, *outlier fraction* η, and $\sigma_{\rm NMAD}$ for each field as a function of number of filters in the fitting (i.e. filter number) in Figure 7-10. For each field *rms*, η and $\sigma_{\rm NMAD}$ get smaller with increasing filter number. However, the achieved improvement is small once at least 8–9 filter bands are available. For these filter bands, the *rms* is $\lesssim 0.15$, $\sigma_{\rm NMAD}$ is $\sim$0.045, and the η is $\lesssim 10$ per cent. The same is true for the *median* $\Delta z/(1 + z_{\rm spec})$ which tends to get smaller and approaches zero the more filter bands are available. We note however, that without the use of the IRAC bands in XMM (thin black long dashed–dotted line), the *median* is slightly offset from zero even with a maximum number of filter bands – a clear indication that the use of the IRAC bands aids the determination of the photometric redshifts. We discuss this in further detail in Section 6.1. In order to provide a better summary view of SERVS as a whole, we also show the 'number-weighted' trends of *rms*, *median*, *outlier fraction* η, and $\sigma_{\rm NMAD}$ derived from all five fields in Figs 7–10 as faint-pink, thick line.[3] Clearly, these are driven by the fields with the most amount of objects available for comparison at any given filter number, thus minimizing the effect of low-number statistics.

As studied in detail already in, e.g. Bolzonella et al. (2000) and Pforr et al. (2013), the quality of the photometric redshifts depends on the number of filters that enter the SED fitting and the wavelength range they cover. We illustrate this for the SERVS fields in Fig. 11. Objects with the best wavelength coverage and most available filter bands are highlighted in the blue, dashed line histogram. For XMM, we have 13 421 objects with detections in all 12 filter bands and χ^2_r<3. The *mean* offset in $\Delta z/(1 + z_{\rm spec})$ for these sources with its one σ scatter is -0.008 ± 0.072 and the *median* is -0.0022. If we consider all objects with a spectroscopic redshift (including those with bad χ^2_r but excluding any for which no photometric redshift could be determined and any with CSNR<3 in either IRAC bands as highlighted before) we find $<\Delta z/(1 + z_{\rm spec})> = -0.032 \pm 0.242$ and a *median* offset of -0.0034. In both cases thepercentage of catastrophic outliers is 2.1 per cent and 8.2 per cent, respectively. The $\sigma_{\rm NMAD}$ are 0.036 and 0.049, respectively.

We list some statistics for each field in Table 6.

[3]We derive these values by multiplying the respective value at each filter number by the number of objects in each field at this filter number, summing all five fields, and then dividing by the total number of objects in all five field at that filter number.

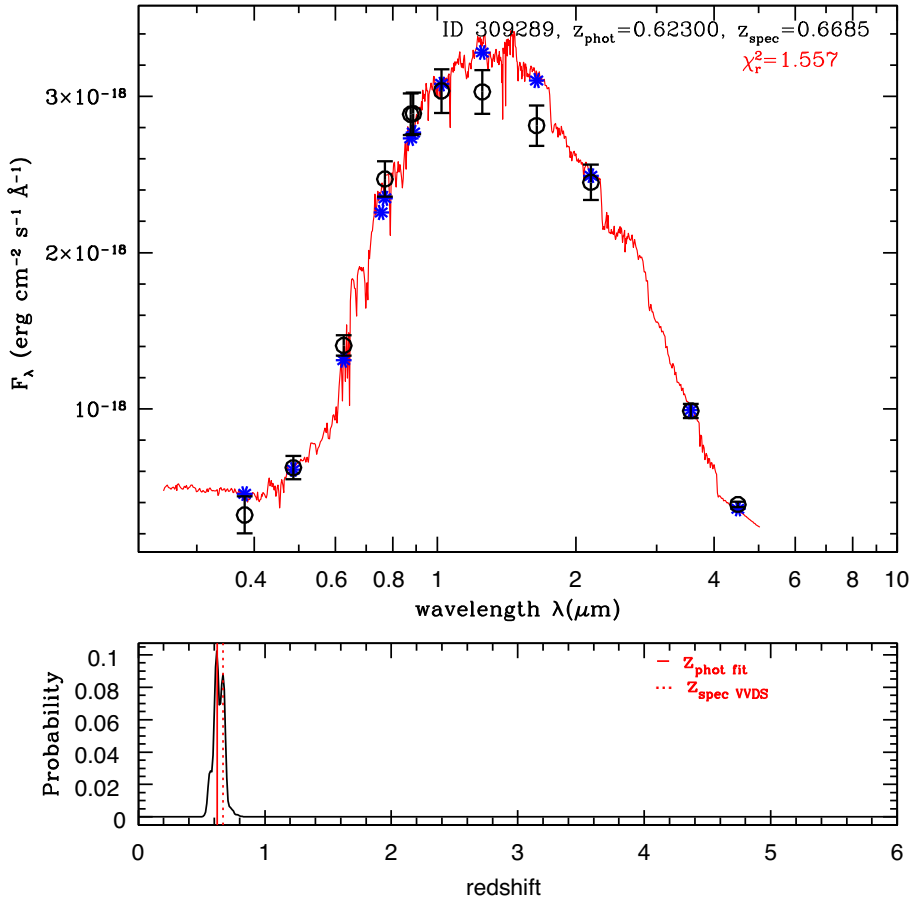

Figure 4. Upper panel: example best-fitting SED template fit (red curve) for object with ID 309289 in the XMM field. Blue asterisks show the predicted fluxes from the template fit in the given filter bands (see Table 3). Black open circles with error bars show the observed flux points in the given filter bands. Listed are the χ^2_r of the fit, the photometric redshift as well as the spectroscopic redshift from the VVDS survey. Bottom panel: PDF(z) for this object (black solid line). The red, dotted vertical line marks the location of the spectroscopic redshift, and the red, solid vertical line that of the derived photometric redshift for this object.

4.1.2 Distinction by survey origin of spectroscopic redshift in XMM

We now carry out the comparison by survey origin of the spectroscopic redshift, i.e. spectroscopic catalogue, focusing on XMM only, since each catalogue has a different definition of redshift quality, covers different redshift ranges, and spectra from the various surveys have different spectral resolutions. The majority of spectroscopic redshifts for our comparison come from the PRIMUS survey (Coil et al. 2011; Cool et al. 2013) and the VIPERS survey (Guzzo & The Vipers Team 2013; Garilli et al. 2014; Scodeggio et al. 2018). The VVDS survey (Le Fèvre et al. 2005) on the other hand provides spectroscopic redshifts out to $z \sim 3.5$ and is a valuable resource to evaluate our photometric redshift quality beyond $z \sim 1$ even though the expected number of SERVS sources at higher redshifts is small. Overall, we find a good agreement between our photometric and the spectroscopic redshifts, particularly for the sources with the widest and most complete wavelength coverage in the available photometry (marked as green points in Fig. 12). We notice that the comparison to spectroscopic redshifts from the PRIMUS DR1 shows the largest scatter. Notably, this is the spectroscopic redshift catalogue with the largest number of $z_{\rm spec}$. The scatter determined from this catalogue is consequently more robustly determined than any scatter determined from catalogues with low number statistics. However, for PRIMUS, we achieve $\sigma_{\rm NMAD} = 0.044$ and $\eta \sim 6$ per cent for objects with 12 available filter bands and a good fit (i.e. $\chi^2_r < 3$). For PRIMUS, the larger scatter likely stems from the low resolution of the spectra ($R \sim 40$; in comparison the resolution achieved with ~30 photometric bands in COSMOS is $R \sim 15-20$; Coil et al. 2011) which results in larger spectroscopic redshift uncertainty compared to conventional spectroscopic surveys. For objects with redshift quality flag ≤ 3, PRIMUS quotes a $\sigma_{\rm NMAD} = 0.0051 \times (1+z)$ and $\eta < 2$ per cent given our definition. The comparison to VVDS, UDSz, and VIPERS shows quite good agreement with a very small η among the objects with the best photometry. We list statistics for the specific catalogues for XMM in Table 6. We stress that although we limit the statistics to objects with $\chi^2_r < 3$, only a small percentage of objects has $\chi^2_r > 10$ as demonstrated in Fig. 13.

For objects with large χ^2_r , it is likely that (1) photometric errors are perhaps too small, (2) one photometric band is offset from the rest due to a significant contribution from a strong emission line, (3) single bands affected by bad or blended photometry that were not filtered out before, (4) AGN features not covered by the galaxy templates we use in the fitting, (5) rare objects with properties outside the parameter range that our setup covers, and/or (6) offsets between the optical MAG_AUTO and the near-IR aperture magnitudes. We discuss some of these options in more detail in Section 6. For objects for which fewer filter bands are available in

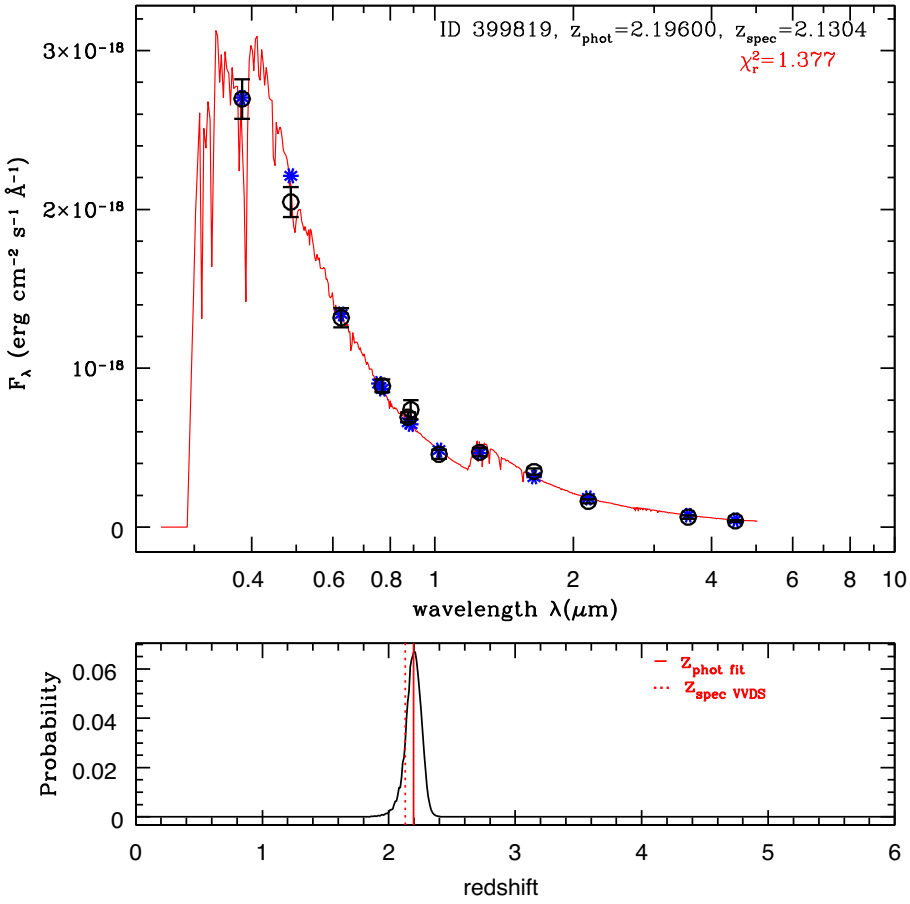

Figure 5. Upper panel: example best-fitting SED template fit (red curve) for object 399819 in the XMM field. Symbols are the same as in Fig. 4. Bottom panel: PDF(z) for this object. The dotted vertical line marks the location of the spectroscopic redshift, and the solid vertical line that of the derived photometric redshift for this object.

the fitting, it is more likely that the χ^2_r will be very small, indicating that the model overfits the data. This is clearly visible in Fig. 13 which shows the peak of the histogram shifting to smaller χ^2_r values with decreasing filter number (top panel) and the overall fraction of objects with $\chi^2_r<3$ at ∼95 per cent compared to ∼65 per cent for objects with more filter bands (bottom panel). Very small χ^2_r are also derived for faint objects which usually have very large photometric errors. Consequently, the PDF(z) of objects with very small χ^2_r will contain several peaks or extended plateaus which means that the photometric redshift determination for such objects is less robust.

We now investigate the same filter band dependencies from Figs 7 to 10 for XMM for each spectroscopic redshift catalogue in Figure 14-17. Globally, we observe the same trends as for ZBEST for each field, meaning *rms*, η, and $\sigma_{\rm NMAD}$ decrease with increasing filter number and the *median* approaches zero for each catalogue and all are smallest on average for the largest available filter number (12 for XMM). We alert the reader that the number of objects at a given number of filter bands can be very small and thus results in either larger than expected or very small *outlier fraction, rms*, and $\sigma_{\rm NMAD}$. For clarity, we list the number of objects contributing to the points for each field at a given number of filter bands in Table 7, but do not display points with less than 20 contributing objects in symbol form. For example, within our restrictions there are only 3 (5) objects with VVDS spectroscopic redshifts with 9 (10) filter bands available in the fitting, 2 (2) of these are catastrophic outliers as per the definition in Section 4, resulting in a spike of higher than expected η, $\sigma_{\rm NMAD}$, *rms*, and negative *median* offset. On the other hand, for eight filter bands there are 0 objects with a spectroscopic redshift from VVDS which is displayed as an *outlier fraction, rms, median*, and $\sigma_{\rm NMAD}$ of 0. Consequently, the high variance in Figs 14–17, especially for less than 10 filter bands, is driven largely by low number statistics. However, besides the small overlap with the Patel et al. (2011) sample, essentially all catalogues contain satisfactory numbers of objects for which 11 and 12 filter bands are available in the fitting. In comparison to the Galaxy And Mass Assembly Survey (GAMA) spectroscopic redshifts which are limited to $z \lesssim 0.5$ (with the majority of the sample at 12 filter bands below z∼0.3) for our sample, we find our photometric redshifts slightly overestimated, resulting in a slightly larger, negative *median* offset, indicating that very low redshifts are not recovered as well even when a large wavelength coverage is available. However, since η is still small, this is not driven by a larger number of catastrophic outliers. We find that while ∼60 per cent of the GAMA galaxies for which 12 filter bands are available are determined by the fit to be older than ∼2.5 Gyr, the remaining are determined by the fit to be between 0.1 and 0.3 Gyr old, many receiving a large dust content. The photometric redshifts are overestimated the most for the sources determined to be young but with a moderate amount of dust of AV<1. These are likely old galaxies in which a small percentage of new star formation

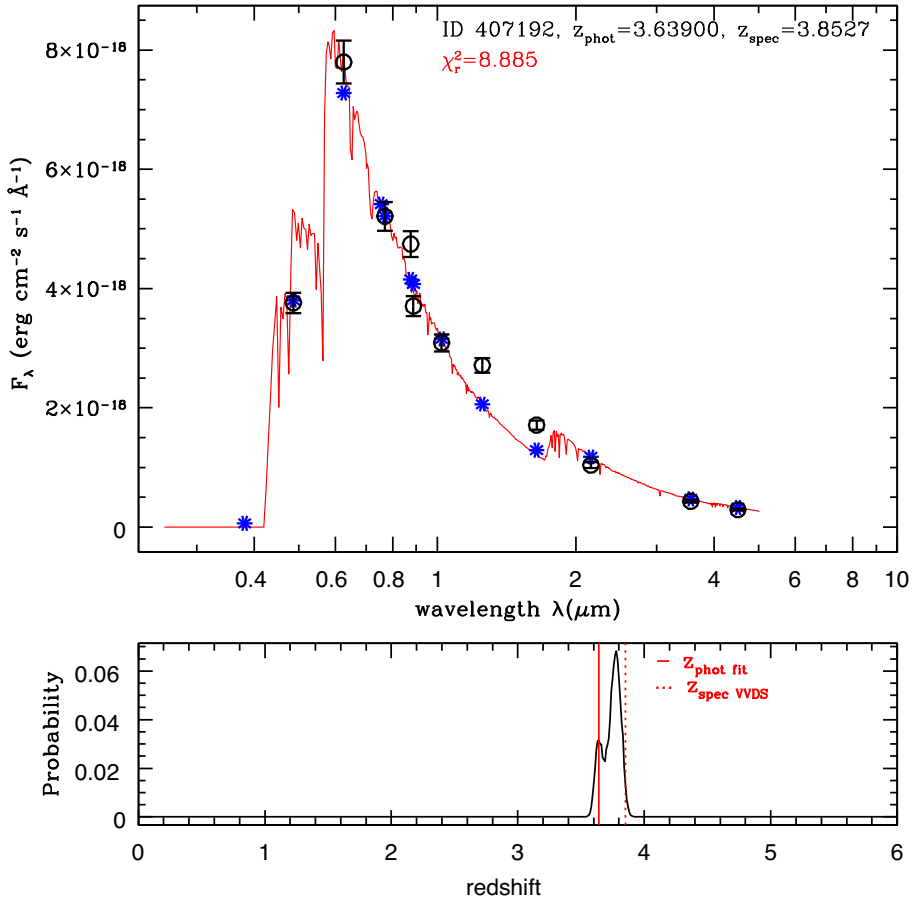

Figure 6. Upper panel: example best-fitting SED template fit (red curve) for object 407192 in the XMM field. Symbols are the same as in Fig. 4. Despite the seemingly bad fit in terms of χ^2_r, the spectral breaks are identified as best as possible and the derived photometric redshift is close to the available spectroscopic redshift. Bottom panel: PDF(z) for this object. The dotted vertical line marks the location of the spectroscopic redshift, and the solid vertical line that of the derived photometric redshift for this object.

overshines the older populations and the slightly larger redshift compensates for excess brightness in the IR stemming from older stellar populations. Rafelski et al. (2015) point out that the addition of near-UV data is particularly helpful in the photometric redshift determination at these low redshifts. We leave further investigation of this effect to future work and future iterations of the SERVS photometric redshifts. For all catalogues and maximum filter bands, we find similar performance: an η <5 per cent, *rms* $\lesssim 0.1$, *median* offset $\sim$0, and $\sigma_{\rm NMAD} \lesssim 0.05$. We provide some of these statistics in Table 6.

4.2 Dependence on *i*-band magnitude

In order to further show the quality of the derived photometric redshifts in each SERVS field and $z_{\rm spec}$ =ZBEST, we display in Fig. 18 both $\sigma_{\rm NMAD}$ and *outlier fraction* η as a function of *i*-band AB magnitude. For ES1 *i* band as used in the following refers to the VIMOS *I* band, and for some objects in XMM to the newer *y* band (see also Table 3). Note that while the individual imaging surveys often go deeper than $i_{\rm AB} = 24$ mag, many of the spectroscopic surveys impose a brightness cut at $i_{\rm AB} = 24$ mag for their samples. For this comparison, we further restricted our sample to objects with at least six filter bands in the fitting since we demonstrated in Figs 7–10 that fits for objects with fewer filter bands are not robust. At the top of the figure, we show the distribution of objects in each field, enhancing those in EN1 and LH by a factor of 10 for visibility. Clearly, for the brightest objects, i.e. $i_{\rm AB} \lesssim 21$, $\sigma_{\rm NMAD}$ lies between $\sim$0.026 and $\sim$0.052 for all fields and then steadily increases with fainter $i_{\rm AB}$ magnitude. Similarly, η increases with fainter $i_{\rm AB}$ magnitude from between $\sim$1 per cent to $\sim$7 per cent for the brightest magnitudes, to more than $\sim$10 per cent for $i_{\rm AB} > 21$ mag. Clearly, the difference in quality and depth of the imaging data and overlap of the various ancillary surveys with each other and with SERVS manifests in more robust photometric redshifts for some fields compared to others. The differences become apparent particularly towards fainter $i_{\rm AB}$-band magnitudes, with EN1 and LH showing less robust photometric redshifts. If we consider the number-weighted average for all SERVS fields, we find $\sigma_{\rm NMAD} \sim 0.04$ and $\eta \sim 4$ per cent for the brightest magnitudes and $\sigma_{\rm NMAD} > 0.05$ and $\eta > 10$ per cent for $i_{\rm AB} > 22.5$.

4.3 Dependence on IRAC 3.6 μm magnitude

In this section, we evaluate if there is a trend between the quality of the derived photometric redshift and the IRAC 3.6 μm magnitude of the object. For this, we show η, $\sigma_{\rm NMAD}$, *rms*, and *median* of $\Delta z/(1 + z_{\rm spec})$ for *XMM* and $z_{\rm spec}$ =ZBEST in different bins of IRAC 3.6 μm AB magnitude in Fig. 19. The distribution of objects as a function of IRAC 3.6 μm AB magnitude is also shown for completeness in the top panel of this figure. We limit ourselves to those

filter#	5	6	7	8	9	10	11	12
XMM	59	83	733	745	3463	1493	6656	13421
$XMM_{no\ IRAC}$	799	809	3622	1631	7756	16182		
XMM_{GOLD}	6	12	296	0	0	3	17	3994
CDFS	2531	4974	1882	2591	1999	1872	673	19
EN1	13	4	32	322	610			
ES1	6	24	71	31	130	341	1514	1371
LH	145	186	1423	511	105			

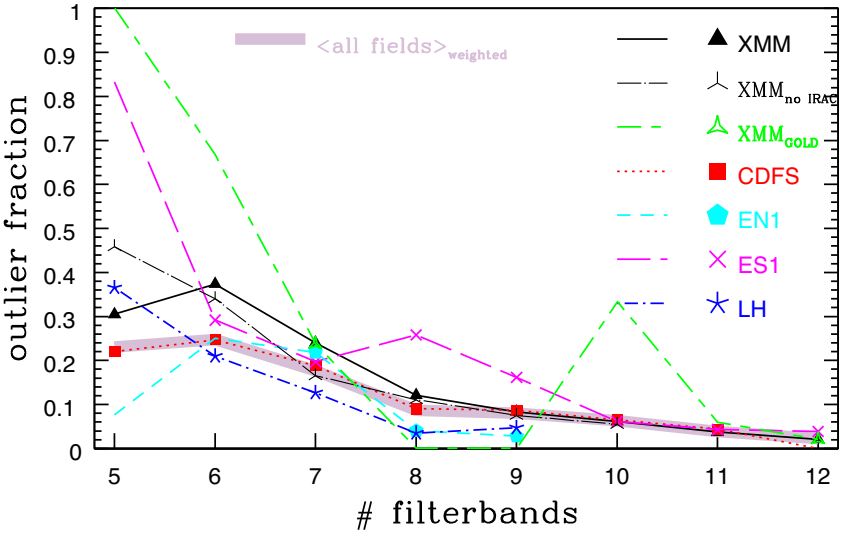

Figure 7. *Outlier fraction* η as function of filter bands for each SERVS field. The maximum number of filters in the catalogues for EN1 (cyan, dashed line and filled pentagons) and LH (blue, dashed–dotted line and stars) is 9, and 12 for the remaining fields XMM (solid, black line and filled triangles), CDFS (red, dotted line and filled squares), and ES1 (magenta, long-dashed line and crosses). For XMM without the two SERVS IRAC bands, the maximum number of filters is 10 (thin, black, long-dashed, dotted line and three-pointed, thin star). For the XMM–GOLD catalogue (green, long-dashed, short-dashed line and thick three pointed star; see Section 6.2), a subset of the full catalogue for which a tighter matching radius to the ancillary data was chosen, the maximum filter number is 12. The average η weighted by the number of objects in each field contributing to the sample with the respective number of filter bands is shown as a thick, faint pink line to show the overall trend for SERVS as a whole. Clearly the fields with the most amount of objects at a given filter band number dominates this average. We list the total number of objects (outliers + non-outliers) with the according number of filter bands available in each field at the top as reference. We only show symbols in addition to the lines when the number of objects for a given field contributing to the point at a given filter band number is larger than 20. While for a small number of available filters, η can be very large since the fit is not very well constrained, a large and consistent wavelength coverage assured by a large number of filter bands from the optical to the IR results in $\eta \sim 5$ per cent (see also statistics in Table 6).

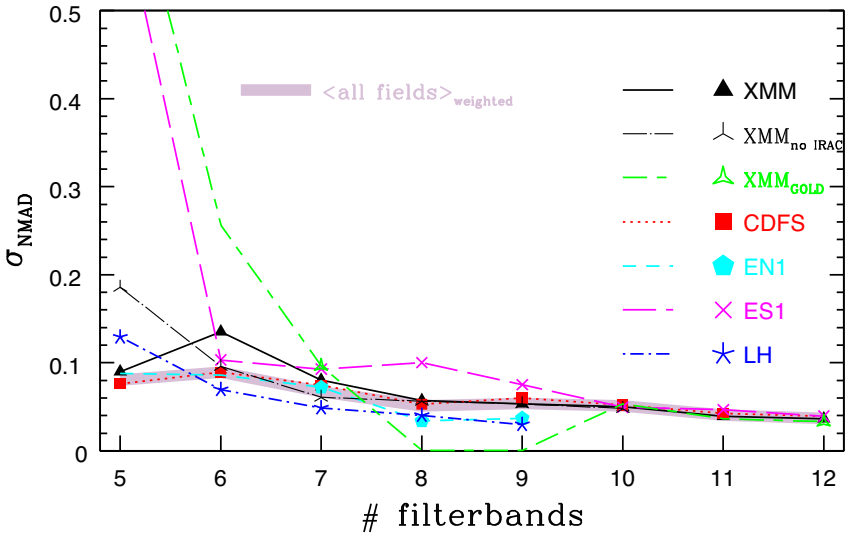

Figure 8. $\sigma_{\rm NMAD}$ as function of filter bands for each of the SERVS fields. Colours, symbols, and line styles are the same as in Fig. 7.

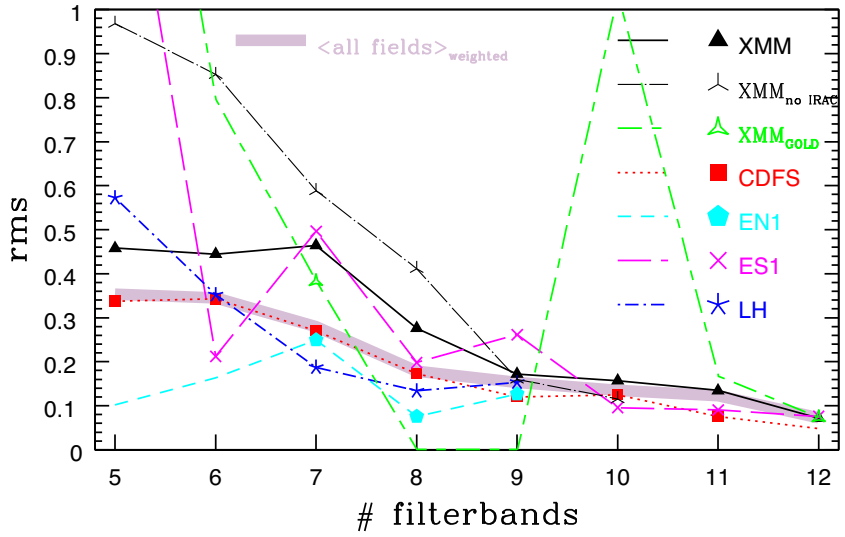

Figure 9. The *rms* as function of filter bands for each of the SERVS fields. Colours, symbols, and line styles are the same as in Fig. 7.

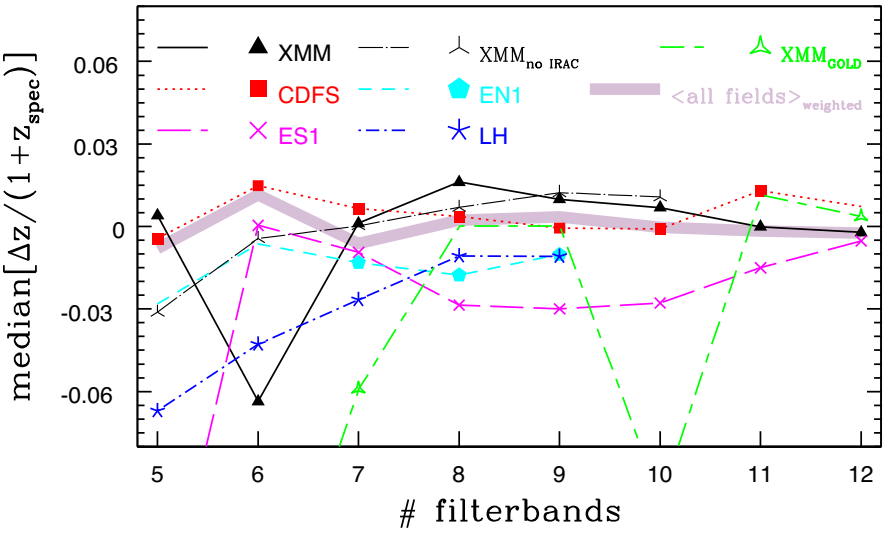

Figure 10. *Median* of $\Delta z/(1 + z_{\rm spec})$ as function of filter bands for each of the SERVS fields. Colours, symbols, and line styles are the same as in Fig. 7.

objects in the magnitude range $18 < m_{3.6\mu{\rm m}} \leq 25$ and for which a good fit could be obtained ($\chi^2_{\rm r}$<3) and CSNR≥3 in both SERVS IRAC bands as described in Section 2.1 from the SERVS DR2 catalogue of which SERVS DR1 is a subset complete down to 23.1 mag (equating to CSNR∼10). We disregard the faintest magnitude bin due to the low number of objects. For objects in the given magnitude range, we can identify a trend such that photometric redshifts are harder to obtain for fainter objects and agree less well with spectroscopic redshifts by a rise in *rms*, *median*, η, and $\sigma_{\rm NMAD}$ at fainter magnitudes.

We then further restrict the sample to only those objects for which more than 10 filter bands are available in the fitting. This ensures that for each object a good amount of photometric data points are available in the fit and a large wavelength coverage exists to reliably determine the shape of the SED and photometric redshift. With this restriction, we are able to investigate whether the previous trend still holds and is not simply the result of a larger fraction of missing photometric data for faint objects. If we only consider magnitude bins brighter than 24 mag in IRAC 3.6 μm then the *median* stays almost constant with magnitude, and the *rms*, η, and $\sigma_{\rm NMAD}$ increase slightly towards IRAC 3.6 μm = 23.5. However, for IRAC 3.6 μm brighter than ∼22.5 mag, $\sigma_{\rm NMAD}$ and η stay almost constant at ∼0.04 and ∼2 per cent, respectively.

This suggests that for example larger photometric errors for fainter objects across the wavelength range still hamper the determination of photometric redshifts. This also suggests that one obvious way to significantly improve our photometric redshift results is to obtain more photometric data points for the sources lacking them through, e.g. using available, deeper observations for smaller parts of the field, applying forced photometry methods to the current data to homogenize the photometry across the ancillary surveys and obtain additional flux measurements. A first attempt of the latter in

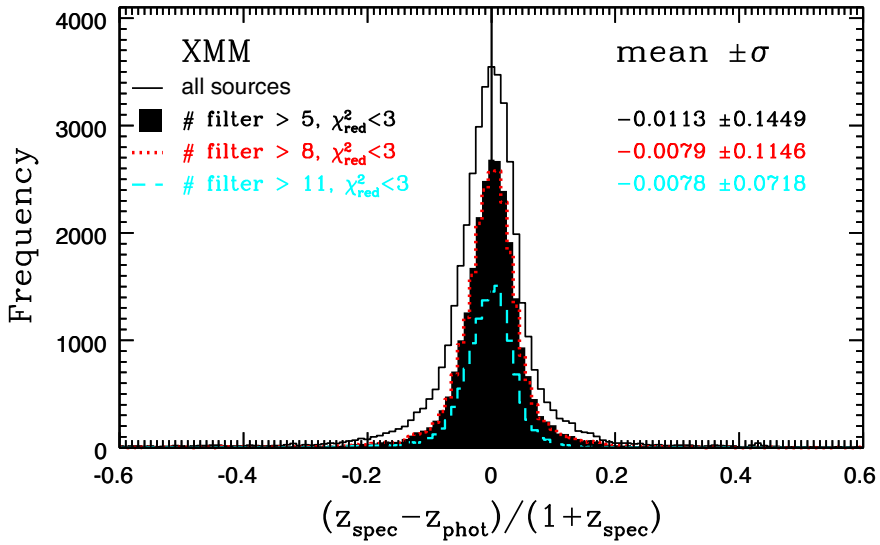

Figure 11. Comparison of photometric redshifts in XMM derived in this work with available high-quality spectroscopic redshifts from the surveys listed in Table 5. z_{spec} refers here to ZBEST, the combination of the best spectroscopic redshifts from various catalogues (see the main text for definition and cuts that were applied). The black line histogram shows the difference in redshifts for all sources with a spectroscopic redshift. The black, shaded histogram restricts the number of objects to those with at least six filter bands available for the SED fitting as well as to those with good fits in terms of χ^2_r <3. The red, dotted line histograms displays the same for objects with at least nine filter bands, and the cyan, dashed histogram for those with 12 filter bands, the maximum number of available filter bands in XMM. It is clear that even the addition of objects with lower filter numbers does not alter the distribution drastically in the sense of offset from 0 or skewedness of the tails towards smaller or large redshifts.

a 1 deg^2 portion of the XMM field is carried out and described in Nyland et al. (2017).

4.4 Dependence on redshift

We further investigate any dependence of our ability to derive good photometric redshifts as a function of redshift itself. Again, we show *outlier fraction* η, σ_{NMAD}, *rms*, and *median* of $\Delta z/(1+z_{spec})$ only for XMM and z_{spec} =ZBEST in different bins of ZBEST in Fig. 20. The distribution of objects as a function of ZBEST is shown for completeness in the top panel of this figure. We limit ourselves to those objects in the redshift range $0 < z \leq 4$ and for which a good fit could be obtained (χ^2_r<3). We find that photometric redshifts for objects between $z_{spec} \sim 0.5$ and ∼1.5 are determined best, while for photometric redshifts below 0.5 and above 1.5, we find larger η, σ_{NMAD}, *rms*, and *median* offsets. For $z < 0.5$, we find a small negative *median* offset, meaning the photometric redshifts are slightly overestimated. We already noted this trend for GAMA sources described in Section 4.1.2.

Our findings are similar when investigating a sample restricted to objects with more than 10 filter bands available in the fitting. It seems that the determination of photometric redshifts of $z > 3$ objects improves again with respect to those in the range of $z_{spec} \sim 1.5-2.5$, but arguably the number of objects with $z_{spec} \geq 1.5$ available for comparison is small.

5 PHOTOMETRIC REDSHIFT DISTRIBUTION

We show the photometric redshift distribution for all of SERVS in Fig. 21. To illustrate the case, we show the redshift distribution only for objects with a filter number larger than five filters, a refined distribution only using objects with more than eight available filters and the CSNR≥3 cut in each IRAC band, and the distribution of the available spectroscopic redshifts in SERVS. The majority of SERVS sources lies between redshift 0 and 1.5 and we observe a tail out to high redshift. Specifically, only 7.2 per cent of all objects in SERVS with at least five available bands in the fitting and 1.5 per cent of all objects with more than eight available bands in the fitting lie above redshift 3 (corresponding to 101 540 and 6169 objects, respectively). However, the determination of robust photometric redshifts for high-redshift objects is more likely to be negatively biased due to very faint or missing detections in the bluest filter bands and consequently a lower number of filter bands available in the fit. Nyland et al. (2017) show that with forced photometry, this negative bias can be corrected and photometric redshifts can be determined robustly for many more objects at high redshift.

Given the depth of SERVS, we expect the high-redshift tail to be dominated by the most massive galaxies at these redshifts, many of which are AGNs or extreme starbursts. We estimate that based on a source density of *Herschel*/SPIRE sources of ∼1/sq arcmin at $z > 1$ we can conservatively expect ∼50 000 of the $z > 1$ objects in SERVS to be starbursts. For AGN, based on the luminosity function estimate of Lacy et al. (2015), we estimate a total of ∼10 000 $z > 2$ AGNs with bolometric luminosities larger than $10^{12}\,L_\odot$ in the 18 deg^2 of SERVS. Some of the SERVS AGN in LH were already studied in Luchsinger et al. (2015) and extremely red, high-redshift objects in SERVS are the object of study in Sajina et al. (in preparation).

6 DISCUSSION

In the following, we will discuss various aspects of the photometry and object types that could affect the photometric redshift determination as described throughout the paper.

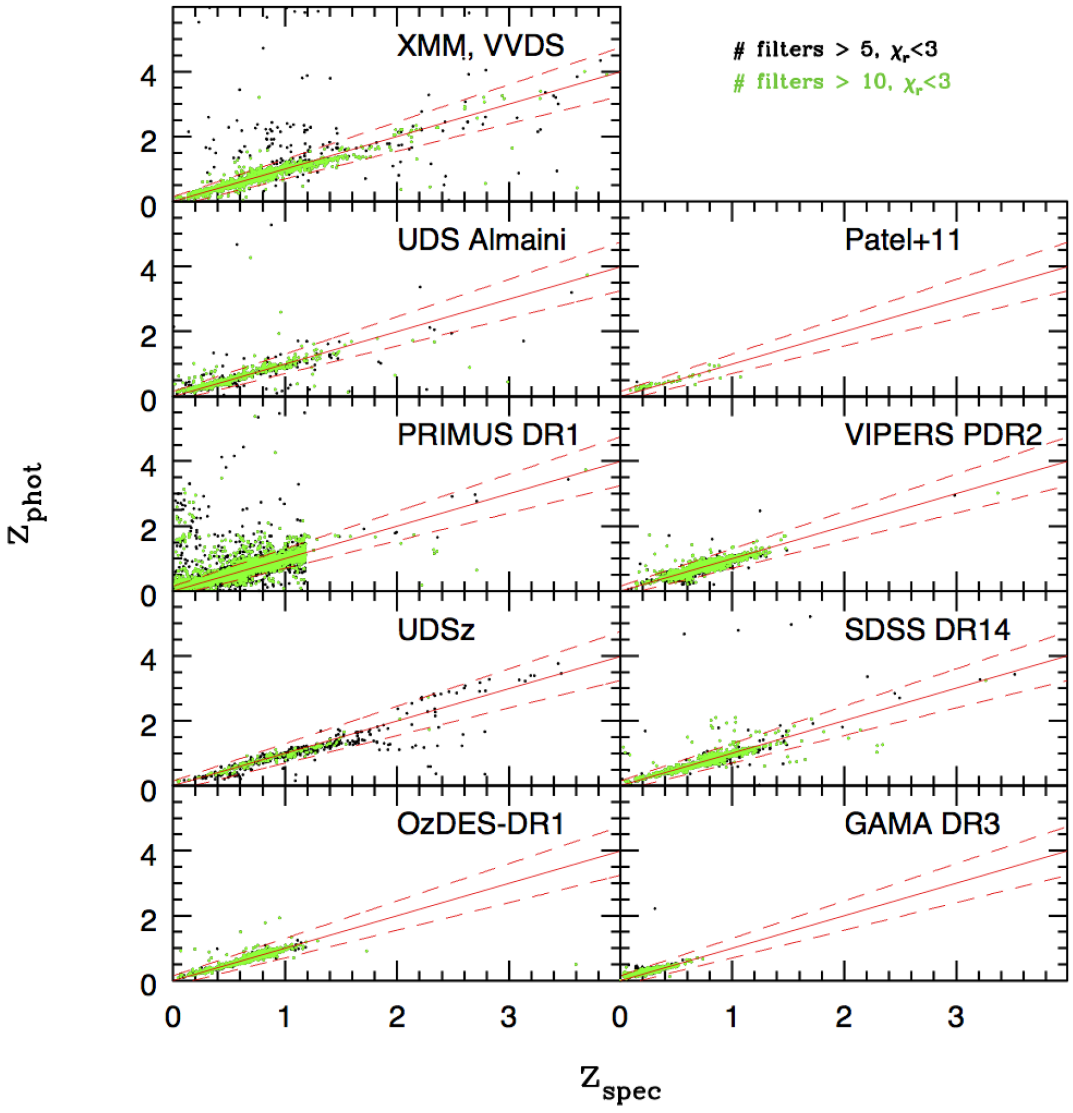

Figure 12. Comparison of photometric redshifts for the XMM field derived in this work with spectroscopic redshifts from various catalogues and surveys. We limit this comparison to those objects with at least six filter bands available for the fitting and a basic fit quality of χ_r^2<3 (black dots). Green dots highlight the sources with the best photometric data, i.e. more than 10 filter bands available, and χ_r^2<3. Red solid lines are lines of equality. Ideally all points would fall on this line. The red dashed lines illustrate the $z_{phot} = z_{spec} \pm 0.15 \times (1 + z_{spec})$ range. Objects outside this range are usually labelled as catastrophic outliers. Quantitative measures of the z_{phot} to z_{spec} agreement for the various z_{spec} source catalogues are listed in Table 6.

6.1 The effects of confusion in the IRAC bands

In order to assess the effect of blending in the IRAC bands which would ultimately lead to an excess brightness in the IRAC photometry for a matched optical/near-IR source and therefore affect the determination of the photometric redshifts, we also calculated the photometric redshifts for XMM without the use of the two SERVS IRAC bands (but still only consider sources that had CSNR≥3 in both IRAC bands). We show some of the results in Figs 22 and 23 and list the statistics in Table 6. Without the use of the IRAC bands, the derived photometric redshifts are skewed towards lower redshifts, especially at $z \lesssim 1.5$, because the IRAC bands serve as long-wavelength range anchor. Additionally, without two filter bands, the number of constraints in the fit is reduced thus allowing more freedom in the fit. Note, however, that since our fitting setup described in Section 3 remains unchanged, and only the number of filter bands was decreased, the χ^2 from these runs could in principle be compared with each other. Here, we simply limit ourselves to the comparison of the resulting photometric redshifts with the spectroscopic redshifts. The comparison to the spectroscopic redshifts shows the same trend in the sense that the photometric redshifts derived without IRAC bands are slightly lower than the spectroscopic redshifts which manifests itself as a small offset in the $\Delta z/(1 + z_{spec})$ distribution towards positive values. We find the *median* offset to be 0.011, the σ_{NMAD} is 0.05 and η 5.5 per cent for the objects with the largest number of filter bands (i.e. 10) and χ_r^2<3. In any case, the IRAC bands become increasingly important at higher redshift where they cover the rest-frame near-IR and optical. Consequently, without the IRAC bands in the fitting η and σ_{NMAD} increase significantly for objects with $z_{spec} > 1.5$, up to 65 per cent and ∼0.4, respectively, similarly to the trends seen in Fig. 20. The *rms* and *median* are also larger at $z_{spec} > 1.5$ than with the inclusion of the IRAC bands.

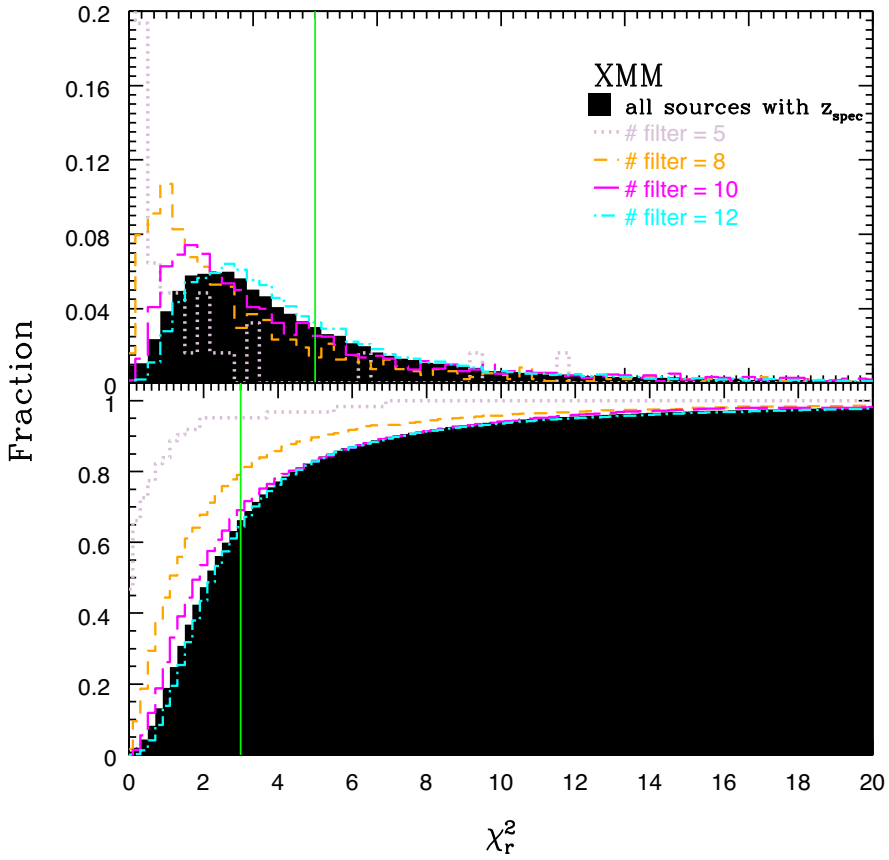

Figure 13. Top: distribution of χ^2_r for sources with spectroscopic redshift in XMM as a function of the number of available filters in the SED fitting (black, shaded histogram). The faint pink, dotted curve shows the histogram if only sources with five filters are considered, the orange, dashed histogram for sources with eight filters, the magenta, long-dashed histogram for sources with 10 filters, and cyan, dashed–dotted histogram for sources with 12 filters. The green vertical line indicates our nominal cut of χ^2_r<3. The χ^2_r is determined as χ^2/(number of filters −1) within HYPERZ (Bolzonella et al. 2000). Bottom: cumulative distribution of χ^2_r in XMM following the colour code from the top panel.

Since the comparison to the z_{spec} has a *median* offset of −0.002 (12 filter bands; 0.007 for 10 filter bands, see also Fig. 10) when the IRAC bands are included in the fitting, which is much smaller than the *median* offset without the IRAC bands, we conclude that the inclusion of the IRAC bands improves the z_{phot} estimation and that source blending in the IRAC bands plays a lesser role for the determination of our photometric redshifts. Using the distribution of the separations of nearest neighbours in the VIDEO K_s-band image that lie within double the angular resolution of SERVS, Nyland et al. (2017) estimated the minimum fraction of sources that are resolved at the resolution of VIDEO but are expected to be blended in the SERVS IRAC images to be ∼17 per cent.

6.2 Improved source cross-matching – the XMM–GOLD catalogue

In order to test whether a tighter matching radius between the IRAC bands and the ancillary catalogues provides a better result for the photometric redshifts by removing wrong and/or multiple matches, we created a 'gold standard' catalogue in XMM (hereafter XMM-GOLD) for which the matching was carried out within 0.7 arcsec radius around the combined SERVS position instead of the 1 arcsec radius. For this purpose, we focused the matching on the XMM–LSS/CFHTLS-deep field, specifically we matched the SERVS source positions to the TERAPIX catalogues (T0007) of the deep, D85 observation in XMM tile 3 (Gwyn 2012). For the photometric redshift determination, we use optical CFHTLS (Canada–France–Hawai'i Telescope Legacy Survey) magnitudes (MAG_AUTO), aperture magnitudes for the VIDEO near-IR bands within 2 arcsec aperture radius and IRAC 1 and 2 aperture magnitudes within 1.9 arcsec radius (see also Table 3). For the XMM–GOLD catalogue both old *i* band and new *i* band (labelled as *y*) were available from CFHTLS for some sources. On average the magnitudes in those two bands agree very well with each other, within their error bars. However, a large discrepancy between the two bands, especially for fainter sources, could result in worse χ^2_r. Therefore, if the source was observed in *i* and *y* bands, we only used the newer observations in the *y* band in the fitting. In all other cases, we kept the *i*-band magnitudes.

The GOLD catalogue contains 168 625 objects. 6505 have spectroscopic redshifts available after we applied the cuts on CSNR etc. as discussed before. If we only consider objects with maximum filter bands (12) and χ^2_r<3, we find for the 3994 objects that fit this criterion a $\sigma_{NMAD} = 0.033$ and η of 2.0 per cent considering ZBEST.

We again derived the statistics for the different spectroscopic catalogues separately. Among the available catalogues, the VVDS survey reaches out to the highest redshifts ($z \sim 3.5$) with a large

Table 6. Overview of the quality of the derived photometric redshifts from the comparison to various spectroscopic redshift catalogues as listed in Table 5. We provide the statistic values when using all objects with available spectroscopic and photometric redshifts as well as the subset with the best photometry and SED-fitting results. *Mean* and *median* values, as well as the 1σ scatter and the *rms* are calculated on $(z_{\rm spec} - z_{\rm phot})/(1 + z_{\rm spec})$. The $\sigma_{\rm NMAD}$ is defined as $1.48 \times {\rm median}[|\frac{(\Delta z - {\rm median}(\Delta z)}{(1+z_{\rm spec})}|]$, and the *outlier fraction* η as $|z_{\rm phot} - z_{\rm spec}| > 0.15 \times (1 + z_{\rm spec})$ (see also the text for a definition for all listed statistics).

SERVS field	Number of filters	Number of objects	*Mean*$\pm 1\sigma$	*Median*	*rms*	$\sigma_{\rm NMAD}$	η
CDFS	≥ 2	20890	-0.047 ± 0.345	0.008	0.348	0.069	0.187
	>10, $\chi^2_{\rm r}<3$	692	0.011 ± 0.074	0.013	0.075	0.043	0.043
EN1	≥ 2	1582	-0.073 ± 0.285	-0.018	0.295	0.042	0.105
	>8, $\chi^2_{\rm r}<3$	610	-0.024 ± 0.125	-0.010	0.127	0.037	0.028
ES1	≥ 2	7496	-0.047 ± 0.257	-0.011	0.261	0.054	0.104
	>10, $\chi^2_{\rm r}<3$	2885	-0.020 ± 0.082	-0.010	0.084	0.042	0.041
LH	≥ 2	3512	-0.132 ± 0.386	-0.032	0.408	0.067	0.205
	>8, $\chi^2_{\rm r}<3$	105	-0.039 ± 0.148	-0.011	0.153	0.030	0.048
XMM	≥ 2	41632	-0.032 ± 0.242	-0.003	0.244	0.049	0.082
	>10, $\chi^2_{\rm r}<3$	20077	-0.010 ± 0.097	-0.002	0.097	0.037	0.026
XMM, VVDS	>10, $\chi^2_{\rm r}<3$	2368	-0.000 ± 0.067	-0.001	0.067	0.038	0.021
XMM, UDS	>10, $\chi^2_{\rm r}<3$	735	-0.020 ± 0.119	-0.011	0.121	0.037	0.048
XMM, Patel et al. (2011)	>10, $\chi^2_{\rm r}<3$	46	-0.028 ± 0.072	-0.044	0.077	0.054	0.065
XMM, PRIMUS	>10, $\chi^2_{\rm r}<3$	15070	-0.013 ± 0.111	-0.003	0.112	0.037	0.031
XMM, VIPERS	>10, $\chi^2_{\rm r}<3$	5311	0.003 ± 0.044	0.005	0.044	0.030	0.006
XMM, UDSz	>10, $\chi^2_{\rm r}<3$	210	0.010 ± 0.044	0.009	0.046	0.039	0.010
XMM, SDSS	>10, $\chi^2_{\rm r}<3$	1519	0.004 ± 0.081	0.012	0.081	0.033	0.022
XMM, OzDES	>10, $\chi^2_{\rm r}<3$	909	-0.004 ± 0.066	0.003	0.066	0.032	0.019
XMM, GAMA	>10, $\chi^2_{\rm r}<3$	1402	-0.037 ± 0.040	-0.036	0.055	0.032	0.010
XMM, no IRAC	≥ 2	41574	-0.094 ± 0.496	0.008	0.505	0.060	0.146
	>9, $\chi^2_{\rm r}<3$	16182	0.014 ± 0.114	0.011	0.115	0.048	0.055
XMM, GOLD	≥ 2	6505	-0.036 ± 0.250	-0.002	0.252	0.045	0.082
	>10, $\chi^2_{\rm r}<3$	4011	-0.002 ± 0.073	0.004	0.073	0.033	0.020
XMM, AGN	>10, $\chi^2_{\rm r}<3$	153	-0.029 ± 0.106	-0.009	0.109	0.042	0.039

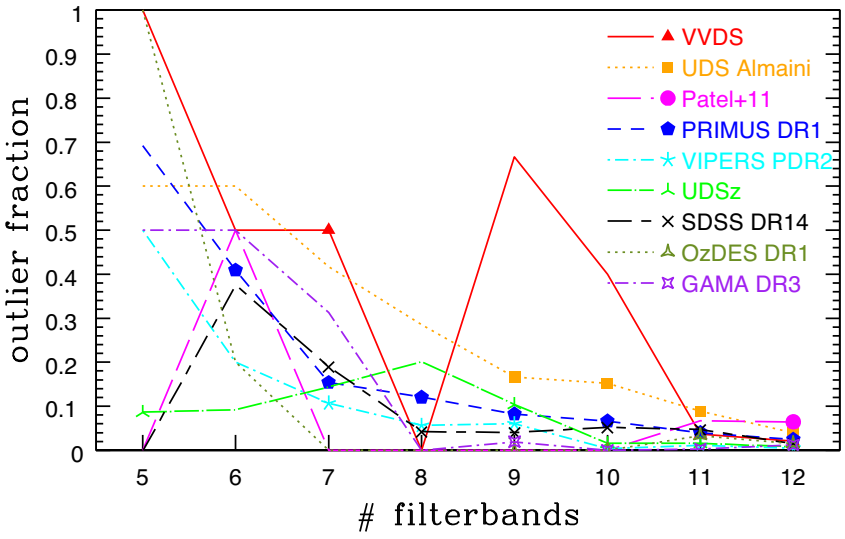

Figure 14. *Outlier fraction* η as function of filter bands and catalogues in XMM. The maximum number of filters for a given catalogue is 12. We distinguish the various sources for spectroscopic redshift by symbol, line colour, and style in the following way: red, solid line and filled triangles for VVDS, orange, dotted line and filled squares for UDS redshifts from Almaini et al., magenta, long-dashed line and filled circles for Patel et al., blue, short-dashed line and filled pentagons for PRIMUS, cyan, dashed–dotted line and five-point stars for VIPERS, light-green, long-dashed dotted line and thin three-point stars for UDSz, black, long-dashed, short-dashed line and crosses for SDSS DR14, olive-green, dotted line and thick three-point star for OzDES, and purple, dashed–dotted line and thick four-point stars for GAMA. We only display symbols along with the lines if the number of objects contributing to the data point contains more than 20 objects to ease the identification of areas affected by low number statistics. Clearly, the high variance especially at low number of filter bands, is due to small number statistics (compare Table 7). However, globally the same trends as in Fig. 7 are observed in that a larger number of available filter bands results in the smallest *outlier fractions* for each catalogue (see also statistics in Table 6).

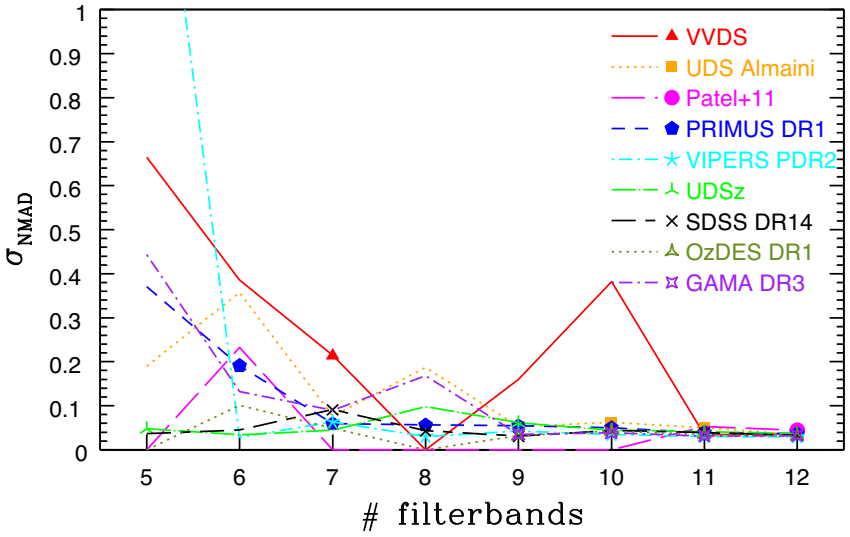

Figure 15. $\sigma_{\rm NMAD}$ as function of filter bands and catalogues in XMM. Line styles, symbols, and colours are the same as in Fig. 14.

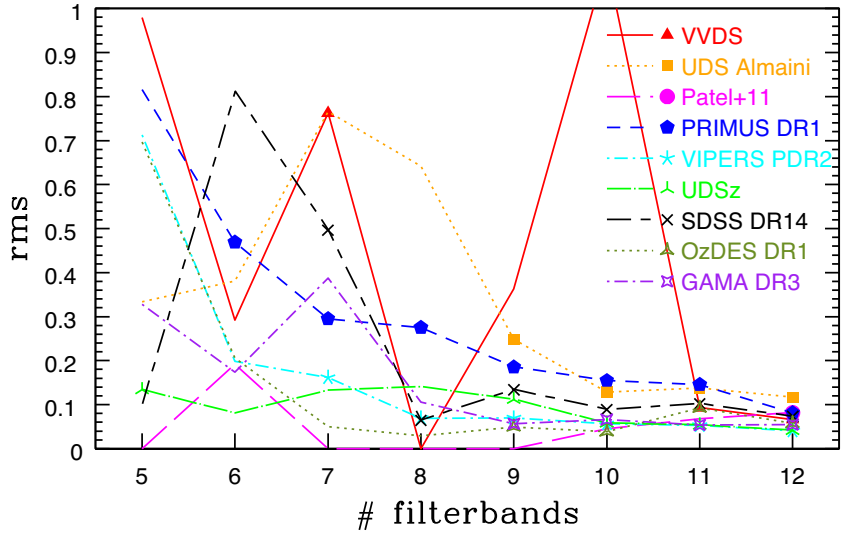

Figure 16. The *rms* as function of filter bands and catalogues in XMM. Line styles, symbols, and colours are the same as in Fig. 14.

fraction of very reliable redshifts (redshift flags 3 and 4). We focus on this particular comparison as the one that provides us with the largest redshift range to test the success of our photometric redshifts. The comparison to the VVDS survey spectroscopic redshifts is shown in Fig. 24 and results in a $\sigma_{\rm NMAD} = 0.031$ with η of 1.4 per cent for objects with the maximum filter bands available and $\chi^2_{\rm r}$ cuts applied as above (2286 objects). Removal of the $\chi^2_{\rm r}$ cut increases the number of objects to 3159, the $\sigma_{\rm NMAD}$ slightly to 0.037 and raises η to ∼3.7 per cent. This is not surprising given the fact that we do not expect a bad fit to return a good photometric redshift. We stress, however, that ∼98 per cent of objects for which the maximum filter bands are available in the fit also receive a best fit with $\chi^2_{\rm r}<10$ and only a small fraction has very bad fits. These could be caused by a variety of reasons which we already mentioned above, such as contribution of an AGN to the optical and near-IR SED. Overall, the comparison to VVDS spectroscopic redshifts is very good, even out to high redshift ($z \sim 3.5$ in this case).

6.3 Photometric redshifts for IR-selected AGN

Our template-fitting setup does not contain AGN templates, consequently we do not expect the photometric redshifts for AGN in the SERVS source catalogues to be accurate by default. However, this is only true if the AGN affects the optical to near-IR SED significantly in any way, for example through the presence of strong or broad emission lines. Our photometric redshifts for ∼60 Ultra-steep Spectrum Radio sources of Afonso et al. (2011) and for radio AGN in LH studied in Luchsinger et al. (2015) showed good agreement with spectroscopic redshifts. Here, we take a closer look at AGN in XMM selected by their IRAC colours. In particular, we use XMM tile 3 which overlaps with VVDS, consists of 188 254 objects, and select AGN in the following way. Starting with the XMM SERVS data fusion, we matched to the VIDEO DR3 within a 1.9 arcsec radius and flagged objects with multiple matches. We then used the AGN wedge (Lacy et al. 2004) to select and flag AGN. The AGN

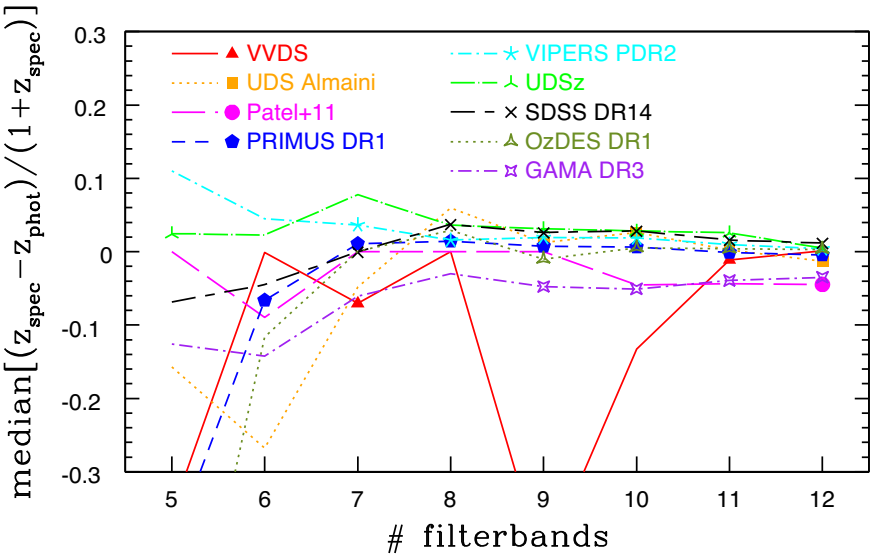

Figure 17. *Median* of $\Delta z/(1+z_{\rm spec})$ as function of filter bands and catalogues in XMM. Line styles, symbols, and colours are the same as in Fig. 14.

Table 7. Overview of the number of objects contributing to each point in Figs 14–17 for a given filter band and spectroscopic redshift catalogue in the SERVS XMM field. The full list of spectroscopic redshift catalogue references can be found in Table 5.

Number of filters	VVDS	UDS Almaini	Patel	PRIMUS	VIPERS	UDSz	SDSS	OzDES	GAMA
$\geq$2, χ_r^2<3	2578	979	49	20383	6253	842	1778	992	1536
5, χ_r^2<3	4	5	0	13	2	35	2	1	2
6, χ_r^2<3	4	5	2	44	5	11	8	5	14
7, χ_r^2<3	188	12	0	429	56	7	37	12	16
8, χ_r^2<3	0	14	0	664	71	20	24	1	2
9, χ_r^2<3	3	120	0	2865	499	300	102	26	52
10, χ_r^2<3	5	46	1	1227	307	68	78	32	39
11, χ_r^2<3	54	124	15	6081	1294	68	390	182	332
12, χ_r^2<3	2314	611	31	8989	4017	142	1129	727	1070

wedge selection is defined as $\log_{10}(S_8/S_{4.5}) \leq 0.8*\log_{10}(S_{5.8}/S_{3.6}) + 0.5$ and $\log_{10}(S_{5.8}/S_{3.6}) > -0.3$ and $\log_{10}(S_{8.0}/S_{4.5}) > -0.3$ and $S_{24} > 200$ μJy using fluxes from the SWIRE survey (Lonsdale et al. 2003). Especially, the 24 μm selection should filter out a lot of high-z starbursts. This selection is targeted towards type-2 AGN which we expect to dominate the AGN population at bolometric luminosities of $\sim 10^{11} L_\odot$. We find 1449 objects which are flagged as AGN candidates this way. 539 out of these have a match to the spectroscopic redshift list detailed in Section 2.2. For these AGN candidates, we show the difference between ZBEST and $z_{\rm phot}$ in Fig. 25. The statistics are listed together with those for the other fields in Table 6. Overall, we find that for these IR-selected AGN our photometric redshifts work reasonably well, though the distribution is slightly skewed towards overestimating their redshift. This is in agreement with the expectation that the optical and near-IR emission of these sources is dominated by their host galaxies rather than the AGN. In order to derive the best photometric redshifts for AGN in general, special treatment for example by using AGN templates in the fitting and including emission lines will be necessary (e.g. Salvato et al. 2009). We will address this in future iterations of our photometric redshifts.

6.4 Star galaxy separation

In this work, we have not excluded potential stars from the sample of SERVS objects. Since our template setup as described in Section 3 does not contain stellar templates we do not expect to derive good fits for any stars in the sample. We provide a colour–colour diagram for each SERVS field in Fig. 26 commonly used to distinguish between stars and galaxies as stars fall within a specified area in these types of diagrams. Here, we chose the differences in the $g-z$ and $z-3.6$ μm magnitudes for XMM, CDFS, LH and EN1, and $V-z$ and $z-3.6$ μm for ES1. Stars can be found in the sequence in the lower right area of the plot. Note however, that the ancillary data in the various SERVS fields can be sparse, e.g. see the low number of sources displayed for the LH field, and not every object has a detection or observational coverage in the selected bands. We therefore leave it to the user of our photometric redshift catalogues to apply their own cuts with respect to star galaxy separation. However, for the comparison to spectroscopic redshifts, this plays a minor role since the majority of sources selected from the spectroscopic surveys are not stars and we restrict our comparison to sources with non-zero spectroscopic redshift and those with χ_r^2<3. However, should

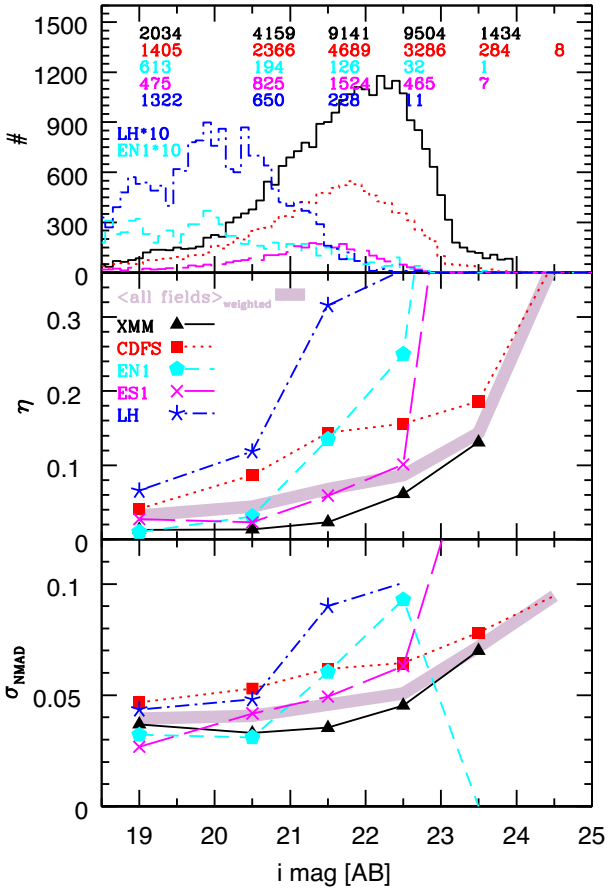

Figure 18. $\sigma_{\rm NMAD}$ (bottom panel), *outlier fraction* η (middle panel), and object number histograms (top panel) as function of *i*-band AB magnitude in magnitude bins of 0.1 mag for each of the SERVS fields. For ES1 *i* band refers to the VIMOS *I* band, and for some objects in XMM to the newer *y* band (see also Table 3). The histograms for EN1 and LH were multiplied by a factor of 10 in order to increase visibility due to low object numbers. We restricted ourselves to sources with CSNR≥3 in both IRAC bands, $\chi^2_{\rm r}$<3 and at least six filter bands in the fitting. η and $\sigma_{\rm NMAD}$ are derived in bins of 1 mag between 20 and 25 mag, and as one single bin for the brightest magnitudes ($i_{\rm AB}$ < 20 mag). We then plot the points at the bin centre and list the number of objects in each bin and field in the top panel. Note that the faintest magnitude bin for EN1 only contains one object, is therefore not representative, and causes $\sigma_{\rm NMAD}$ to be zero. Colours, line styles, and symbols are the same as in Fig. 7.

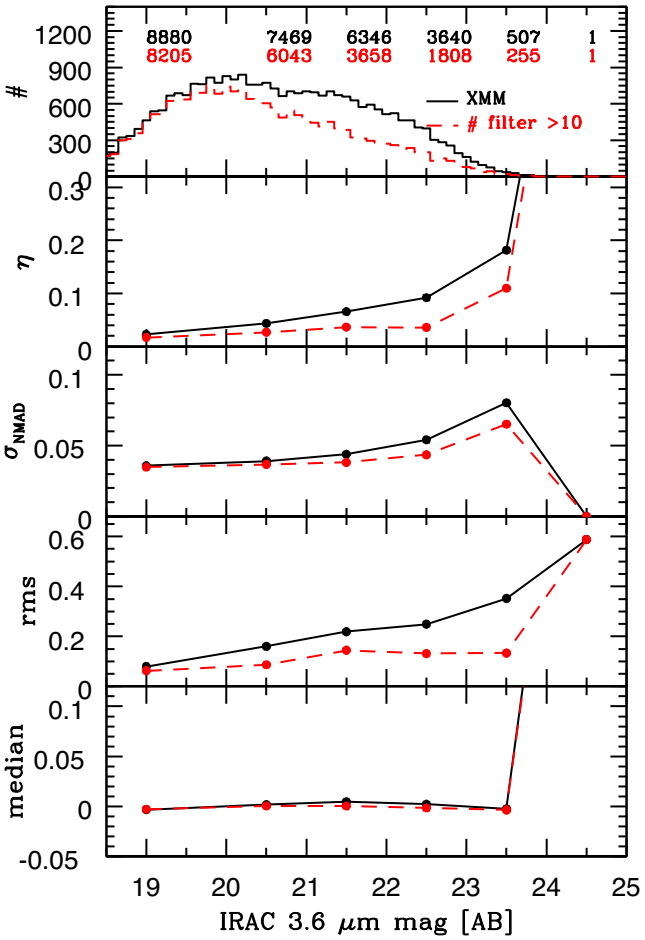

Figure 19. From top to bottom: magnitude distribution in bins of 0.1 mag, *outlier fraction* η, $\sigma_{\rm NMAD}$, *rms*, and *median* of $\Delta z/(1+z_{\rm spec})$ as a function of IRAC 3.6 μm AB magnitude for objects with 18 < IRAC 3.6 μm ≤25 mag and $\chi^2_{\rm r}$<3 for which a spectroscopic redshift is available. η, $\sigma_{\rm NMAD}$, *rms*, and *median* are derived in bins of 1 mag between 20 and 25 mag, and in bins of 2 mag for the brightest magnitudes (18–20 mag). We then plot the points at the bin centre and list the number of objects in each bin at the top in the top panel for the two samples. Note that the faintest magnitude bin only contains one object, is therefore not representative, and causes $\sigma_{\rm NMAD}$ to be zero. The black points and lines show the values for all objects in that magnitude and $\chi^2_{\rm r}$ range; and the red points and dashed red lines show the values for a sample that is further restricted to objects which have more than 10 filter bands available in the fitting. A clear trend exists in all panels such that photometric redshifts agree less well with spectroscopic redshifts as IRAC 3.6 μm magnitudes become fainter. Note that SERVS DR1 is complete down to 23.1 mag (equating to roughly CSNR=10), but in this figure, we consider all objects from SERVS DR2 with CSNR≥3 in both SERVS IRAC bands which allows us to go slightly fainter.

any stars still be present in the comparison sample, we expect our statistics to be minimally affected and to at best improve and at worse remain the same once any remaining stars are removed.

7 COMPARISON TO THE LITERATURE

Photometric redshifts are routinely derived for every large galaxy survey resulting in a myriad of publications. Here, we will limit ourselves to comparing our result to a few, recent studies that are often considered to present the most accurate photometric redshifts from template SED fitting.

First, our results agree with general findings that the larger the number of available filter bands and especially wavelength coverage in the fitting, the lower the fraction of catastrophic outliers (e.g. Bolzonella et al. 2000; Ilbert et al. 2006; Rowan-Robinson et al. 2008; Ilbert et al. 2009; Pforr et al. 2013; Rowan-Robinson et al. 2013; Rafelski et al. 2015). Additionally, Rowan-Robinson et al. (2008) – who derived photometric redshifts for ∼1 000 000 galaxies in the same five fields in the framework of the SWIRE survey using 0.36 to 4.5 μm broad-band fluxes by employing a mix of seven galaxy templates (elliptical, spiral, and starbursting galaxies) and 3 AGN templates – also found that the inclusion of IRAC bands in the fitting significantly lowers the fraction of outliers (for updated photometric in SWIRE, see also Rowan-Robinson et al. 2013). Table 6 shows that our results agree with this finding.

Second, e.g. Ilbert et al. (2009) clearly show that their $\sigma_{\Delta z/(1+z_s)}$ (i.e. NMAD) are smallest for brighter galaxies. Ilbert et al. (2009)

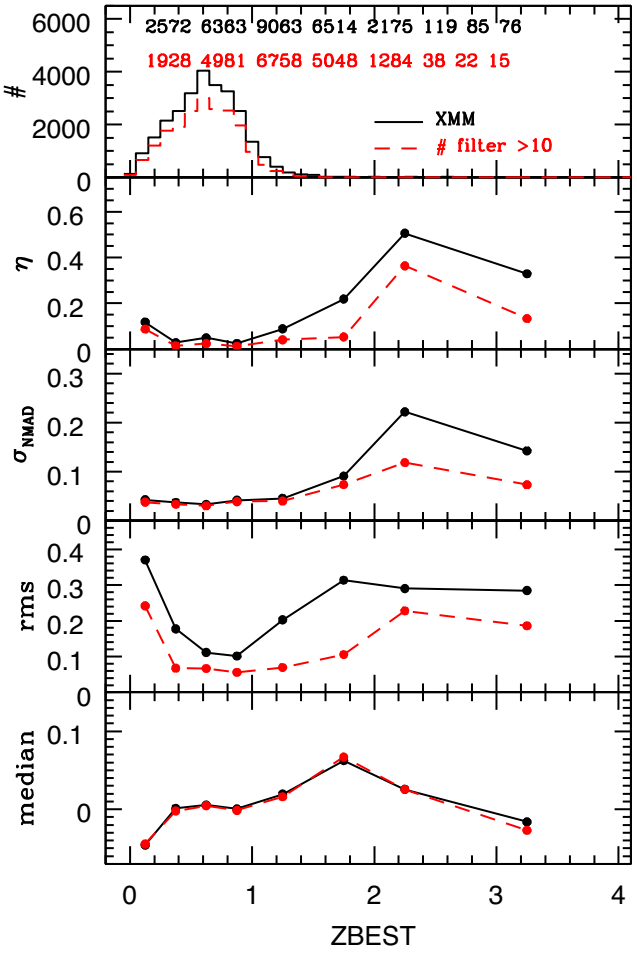

Figure 20. From top to bottom: spectroscopic redshift distribution in bins of 0.1, *outlier fraction* η, $\sigma_{\rm NMAD}$, *rms*, and *median* of $\Delta z/(1+z_{\rm spec})$ as a function of spectroscopic redshift ZBEST for objects with $0 < z \leq 4$ and $\chi^2_{\rm r}$<3 for which a spectroscopic redshift is available. η, $\sigma_{\rm NMAD}$, *rms*, and *median* are derived in bins of 0.25 between $0 < z \leq 1$, in bins of 0.5 between $1 < z \leq 2.5$, and for the highest redshift bin from $2.5 < z \leq 4$. We then plot the points at the bin centre and list the number of objects in each bin at the top in the top panel for the two samples. The black points and lines show the values for all objects in that redshift and $\chi^2_{\rm r}$ range; the red points and dashed red lines show the values for a sample that is further restricted to objects which have more than 10 filter bands available in the fitting.

used 30 medium filter bands in the COSMOS 2 deg^2 extragalactic field to obtain photometric redshifts with the LEPHARE code (Ilbert et al. 2006; Arnouts et al. 1999) for about 600 000 galaxies. Their photometric redshifts have an accuracy of $\sigma_{\Delta z/(1+z_s)} = 0.007$ for galaxies brighter than $i^+_{\rm AB} < 22.5$ and $\sigma_{\Delta z/(1+z_s)} = 0.012$ for galaxies at $i^+_{\rm AB} \sim 24$ at $z < 1.25$ ($\sigma_{\Delta z/(1+z_s)} = 0.06$ for $z \sim 2$). While a wide wavelength coverage with broad-band photometry alone, as is the case in this paper, achieves robust photometric redshifts by tracing the overall SED shape and identifying prominent spectral breaks, a finer sampling of the SED shape with medium or narrow filter bands as in the case of Ilbert et al. (2009) results in higher accuracy of the photometric redshifts. Ilbert et al. (2009) compare their 30 band photometric redshifts with those from the CFHTLS–DEEP survey (Ilbert et al. 2006) which utilizes only five broad bands from $u*$ to z' band and find an improvement of a factor of 3 in photometric redshift accuracy. In their case of fitting to medium bands in addition to broad bands, the inclusion of emission lines in the template fitting is important since the presence of a strong emission line affects magnitudes derived from medium and narrow filter band observations relatively more due to the narrower wavelength range covered by the filter width. Ilbert et al. (2009) find an improvement of a factor of 2.5 in photometric redshift accuracy when including emission lines in the fitting which includes medium filter bands. With updated near-IR data, they achieve $\sigma_{\Delta z/(1+z_s)} = 0.03$ for galaxies between $1.5 < z < 4$ (Ilbert et al. 2013). Splitting our sample in XMM into the same magnitude bins in Canada–France–Hawaii Telescope (CFHT) *i*-band AB magnitude we obtain $\sigma_{\rm NMAD} = 0.038$ and 0.056, for the bright and faint samples, respectively, across our entire redshift range. If we consider the number-weighted values for $\sigma_{\rm NMAD}$ across all SERVS fields (see Section 4.2 and Fig. 18), we find $\sigma_{\rm NMAD} \sim 0.04$ for the brightest magnitudes and $\sigma_{\rm NMAD} > 0.05$ for $i_{\rm AB} > 22.5$. Since most of the galaxies in SERVS are located at redshifts $z < 1.5$ and most available spectroscopic redshifts for our comparison are below $z < 1$, limiting the redshift to $z < 1.25$ for the faint sample to compare to the Ilbert et al. (2009) values will not alter these conclusions. We thus agree on the trend that photometric redshifts are better determined for brighter galaxies. Overall, unsurprisingly our values of $\sigma_{\rm NMAD}$ are worse than those of Ilbert et al. (2009) partly due to the limitations inherent to the photometric data available for our sources. Our data are limited to a few broad filter bands across a wide wavelength range resulting in a much lower 'resolution' of the galaxy SED shapes and much more inhomogeneous across the ancillary surveys.

Recently, the approach taken by the CANDELS team of combining and taking the *median* of the photometric redshifts from several different codes was found to provide a better result than each single code (Dahlen et al. 2013). Using forced photometry (employing TFIT, Laidler et al. 2007; Galametz et al. 2013; Guo et al. 2013), they find $\sigma_{\rm NMAD} = 0.025$ and η of 3.1 per cent.

Rafelski et al. (2015) on the other hand derive photometric redshifts in the Hubble Ultra Deep field including new near-UV data, but without *Spitzer* data, using aperture-matching and point spread function (PSF) correction for their space-based only, 11 band photometry, employing BPZ (Benítez 2000) and EAZY (Brammer, van Dokkum & Coppi 2008). Overall, they find $\sigma_{\rm NMAD} \sim 0.029$ and $\eta \sim 3.8$ per cent. They find that their new method of treating photometry and the extension to near-UV wavelengths improves on previous redshifts by a factor of 2 in $\sigma_{\rm NMAD}$ and nearly a factor of 3 in η in total. In particular, they find that the addition of the NUV data improves the estimation at $z < 0.5$. Their $\sigma_{\rm NMAD}$ and η are somewhat better than our results when IRAC bands are excluded from the fit which is not surprising given their deeper, space-based *Hubble Space Telescope* (*HST*) photometry, aperture matching and PSF correction. However, our results for objects with the largest number of filters available are comparable in terms of $\sigma_{\rm NMAD}$ and η.

As described in Nyland et al. (2017) on the example of 1 deg^2 in the XMM field, the SERVS team is using THE TRACTOR image modelling code (Lang, Hogg & Schlegel 2016) to perform forced photometry that will ultimately lead to more accurate multi-band source catalogues and photometric redshifts in the future.

8 SUMMARY

In this paper, we present the photometric redshifts for sources detected in the 18 deg^2 SERVS at 3.6 and 4.5 μm in the five extragalactic fields ES1, EN1, LH, XMM−LSS, and CDFS. We describe the derivation method based on template SED fitting following our

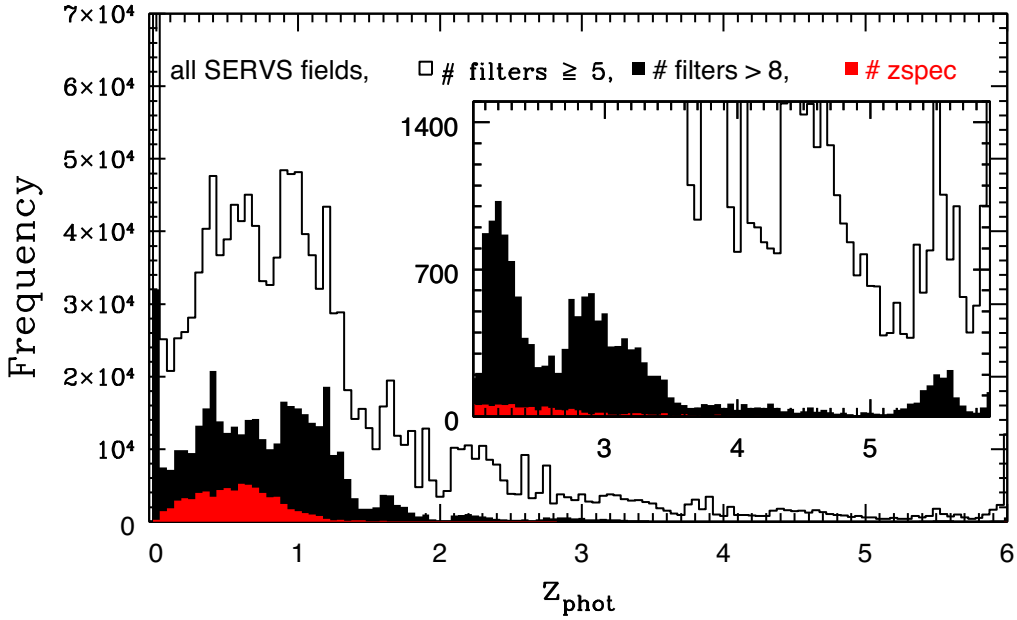

Figure 21. Photometric redshift distribution for all SERVS fields combined, considering only sources with more than eight filter bands in the SED fitting and applying a CSNR≥3 cut in both IRAC bands (black, shaded histogram) and for all sources with more than five filter bands available for the fitting and without CSNR cuts (solid, black line histogram). Clearly, the majority of SERVS sources lies below $z \sim 1$ and only a few sources are located at higher redshifts. As reference, we also show the distribution of the sources in our spectroscopic redshift comparison sample in all SERVS fields (see Table 5) in the red, shaded histogram.

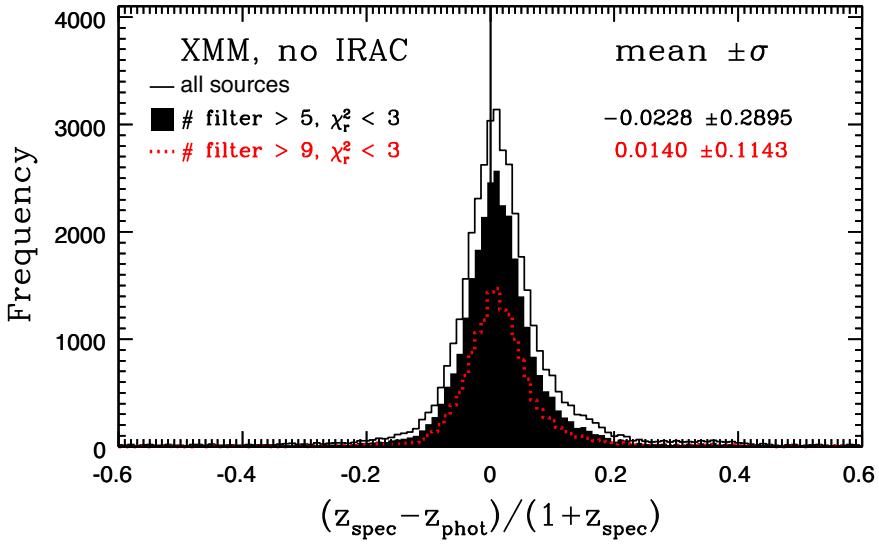

Figure 22. Comparison of photometric redshifts in XMM derived in this work without using the IRAC bands with available high-quality spectroscopic redshifts from the surveys listed in Table 5. The black line, empty histogram shows the difference in redshifts for all sources with a spectroscopic redshift and the cuts discussed in the main text. The black, shaded histogram shows the number of objects with more than five filter bands in the fitting and with good fits in terms of χ^2_r<3. The red, dotted line histogram shows the sample restricted further to only sources with 10 filter bands, the maximum number of filter bands in XMM without the IRAC bands, available for the SED fitting. Compare to Fig. 11 for the results including both IRAC bands in the fitting.

most economic setup as described in Pforr et al. (2013). We describe the available multiwavelength data from ancillary sources as well as the available spectroscopic redshifts. We use the latter for the evaluation of the accuracy and success of our photometric redshifts and employ standard statistical values to estimate photo-z accuracy and compare our results to the literature. We illustrate how the reliability of the photometric redshifts depends on the number of available filter bands in the fitting and source brightness, and show comparisons between photometric and spectroscopic redshifts for a variety of spectroscopic redshift surveys, as a function of the number of filter bands, as a function of i band and IRAC 3.6 μm magnitude and as a function of spectroscopic redshift. We discuss the effect of excluding the IRAC bands in the fitting on the photometric redshifts and discuss ways to improve the photometric redshifts through improvement of the photometry via e.g. tighter source matching radius. We also briefly highlight the redshift success for type-2 IR-selected

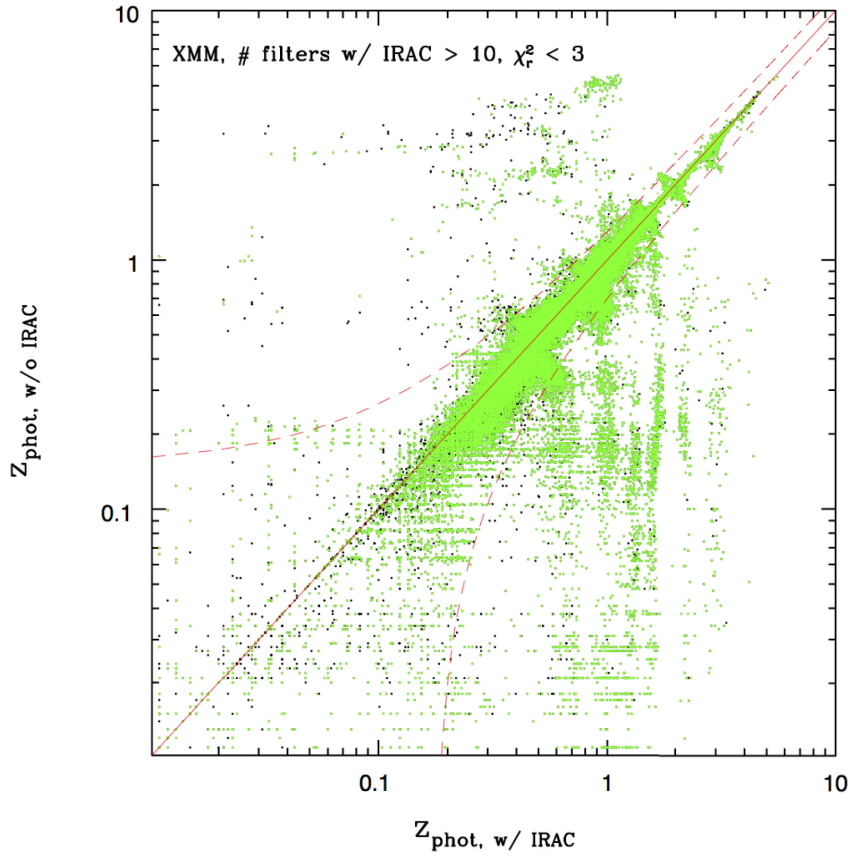

Figure 23. Comparison between derived photometric redshifts in XMM for inclusion and exclusion of the IRAC bands in the fitting. Black dots show all objects with a good fit in both cases (i.e. χ^2_r<3), and the green dots only show objects with the additional restriction of CSNR≥3 in both IRAC bands.

AGN given that our template-based fitting only consists of galaxy templates without AGN contribution. Our results on these topics can be summarized as:

(i) In general, the more photometric filter bands over a large wavelength range are available for the fitting, the robuster the photometric redshifts, i.e. the smaller $\sigma_{\rm NMAD}$, *outlier fraction* η, *rms*, and *median* difference. Photometric redshift accuracy is further improved by a fine sampling of the SED with medium and narrow filter bands in the fitting.

(ii) For large numbers of filter bands and excluding objects with $\chi^2_r \geq 3$ $\sigma_{\rm NMAD}$ varies between 0.030 and 0.043 and η between 2.6 and 4.8 per cent between the five SERVS fields due to the different ancillary data sets.

(iii) For large numbers of filter bands and excluding objects with $\chi^2_r \geq 3$ $\sigma_{\rm NMAD}$ varies between 0.03 and 0.054 and η between 0.6 and 6.5 per cent between the different spectroscopic redshift catalogues available for comparison in XMM.

(iv) Excluding IRAC bands in the fitting for XMM results in an increase of $\sigma_{\rm NMAD}$ to 0.048 and η to 5.5 per cent considering ZBEST with $\chi^2_r \geq 3$, compared to $\sigma_{\rm NMAD} = 0.037$ and 2.6 per cent with the inclusion of IRAC bands, respectively. The exclusion of IRAC bands results in a median small underestimation of photometric redshifts (*median* difference of 0.013 in $(z_{\rm spec} - z_{\rm phot})/(1 + z_{\rm spec})$).

(v) Applying a tighter matching radius of 0.7 arcsec compared to 1 arcsec in a small part of XMM improves $\sigma_{\rm NMAD}$ to 0.033 and η to 2.0 per cent considering ZBEST with $\chi^2_r \geq 3$ due to fewer spurious matches.

(vi) In general, $\sigma_{\rm NMAD}$, η, *rms*, and *median* difference increase with fainter $i_{\rm AB}$-band magnitude for all SERVS fields. Specifically, we find $\sigma_{\rm NMAD} \sim 0.04$ and $\eta \sim 4$ per cent for the brightest magnitudes and $\sigma_{\rm NMAD} > 0.05$ and $\eta > 10$ per cent for $i_{\rm AB} > 22.5$.

(vii) In general, $\sigma_{\rm NMAD}$, η, *rms*, and *median* difference increase with fainter IRAC 3.6 μm AB magnitude. This effect is partly due to missing detections in bluer bands of shallower surveys and partly due to larger photometric errors at fainter magnitudes which hamper tighter constraints in the fitting. When selecting only sources with large numbers of available filter bands we do not observe this trend with IRAC 3.6 μm AB magnitude.

(viii) Generally, $\sigma_{\rm NMAD}$ and η are lowest at $z \lesssim 1$ and increase towards $z \sim 2$ which agrees with the previous point since higher redshift sources are generally expected to lack photometric detections in bluer bands due to the shifted spectrum and fainter brightnesses due to increased redshift.

(ix) At $z < 0.5$, the *median* difference between photometric and spectroscopic redshift is such that photometric redshifts are slightly overestimated, at $z > 1$ the *median* difference indicates that photometric redshifts are slightly underestimated.

(x) We find the majority of SERVS sources (∼76 per cent with at least five available filter bands) below $z < 1.5$ and 1.5 per cent of objects with at least eight filter bands in the fitting to lie at $z > 3$ (∼7 per cent of sources with at least five filter bands in the fitting).

Overall, despite the inhomogeneity of the input catalogues, our photometric redshifts are reliable (using >5 filter bands over a wide wavelength range in the SED fitting), demonstrating that even with-

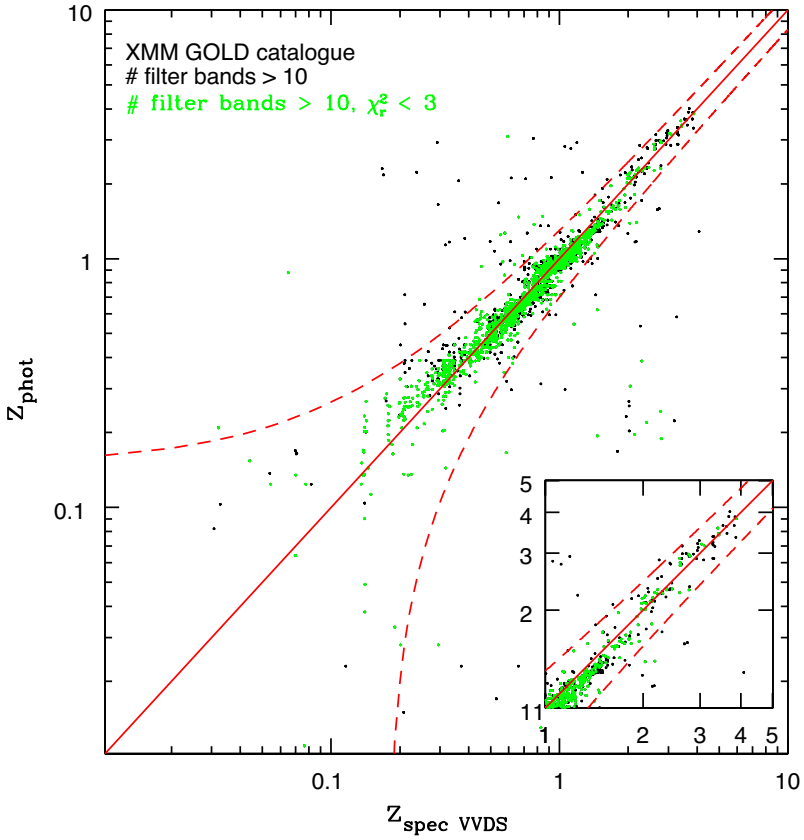

Figure 24. Comparison of photometric redshifts derived for the XMM–GOLD catalogue to VVDS spectroscopic redshifts. The different colours refer to different cuts applied to the sample. In black, we show only those that have more than 10 filters available in the fitting, and in green, we highlight the ones with more than 10 filters in the fitting and a χ^2_r<3. The red solid line is the line of equality, and the red dashed lines mark the border for catastrophic outliers. The inset shows the region around $1 < z < 5$ enlarged.

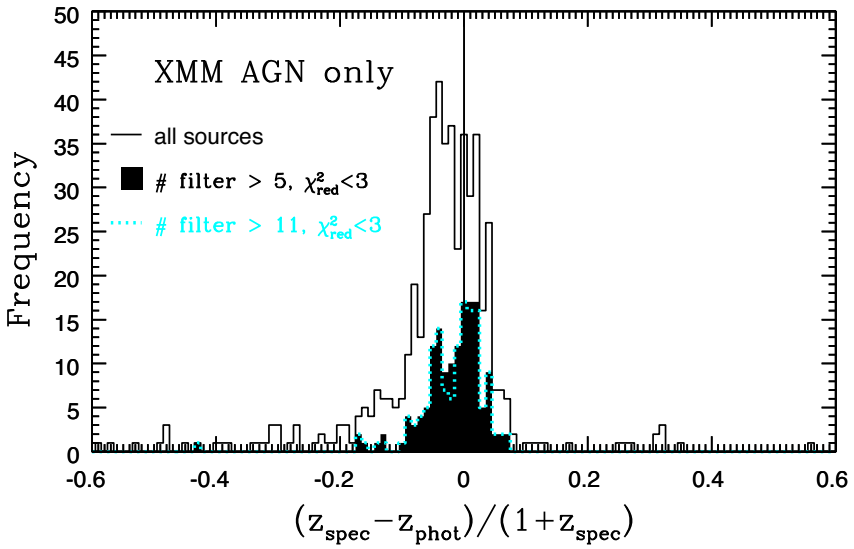

Figure 25. Comparison of photometric redshifts for AGN candidates in XMM derived in this work with available high-quality spectroscopic redshifts from the surveys listed in Table 5. The empty, black line histogram shows the difference in redshifts for all sources with a spectroscopic redshift given the cuts listed in Section 2.3. The black, shaded histogram restricts the number of objects to those with more than five filter bands available in the fitting and good fits, i.e. χ^2_r<3, the cyan, dotted-line histogram further restricts this sample to objects with 12 filter bands, i.e. the maximum number, in the fitting. Compare to Fig. 11 for the results for all objects in XMM.

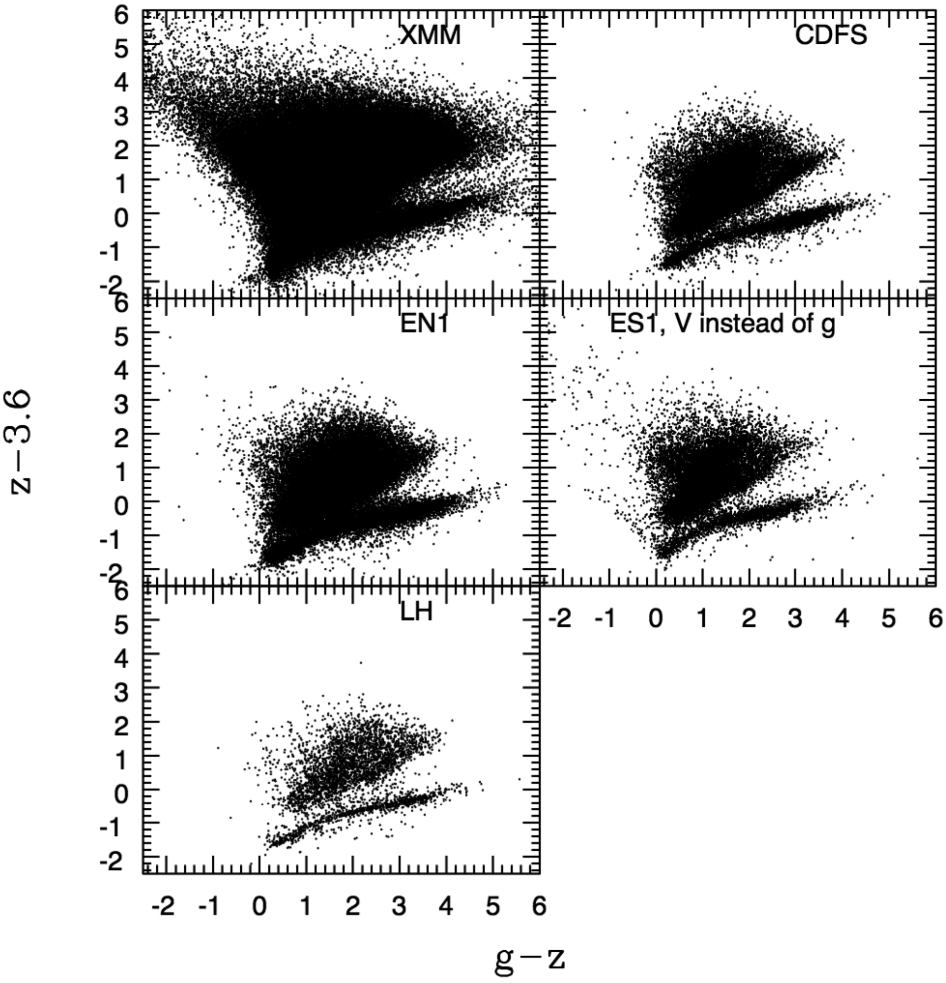

Figure 26. $g-z$ versus $z-3.6$ μm colour–colour diagrams for each SERVS field to illustrate star galaxy separation. Stars can be found in the lower right part of each panel. Note that for ES1, we use $V-z$ instead of $g-z$. Also note that the coverage of the optical ancillary surveys is sparse in some fields which naturally affects the number of objects displayed in these. We only show objects which have a detection in each of the three bands used to calculate the two colours.

out more difficult reprocessing of photometry photometric redshifts useful for science analyses can be obtained. Nevertheless, we strive to further improve the photometric redshifts for SERVS and its extension survey DEEPDRILL (PI: M. Lacy) in the future.

ACKNOWLEDGEMENTS

The authors would like to thank the referee for their thoughtful and detailed comments which further improved the content of this publication. We would like to extend special thanks to M. Bolzonella for continued support of the HYPERZ fitting code. We thank Anna Sajina and the rest of the SERVS team for helpful discussions improving the content and presentation of this paper. This work was partly supported by the Marie Curie Excellence Team Grant UniMass MEXT-CT-2006-042754 (PI: C. Maraston), by HST programme GO-12060, support for which was provided by NASA through a grant from the Space Telescope Science Institute, which is operated by the Association of Universities for Research in Astronomy, Inc., under NASA contract NAS 5-26555, and by funding from the European Research Council Advanced Grant ERC-2010-AdG-268107-EARLY (PI: O. Le Fèvre). JP is supported through an ESA Research Fellowship. MV and LM acknowledge support from the European Commission Research Executive Agency (FP7-SPACE-2013-1 GA 607254), the South African Department of Science and Technology (DST/CON 0134/2014) and the Italian Ministry for Foreign Affairs and International Cooperation (PGR GA ZA14GR02). LM acknowledges support from the South African National Research Foundation (NRF) through the South African Research Chairs Initiative (SARChI). KN is supported by a grant associated with Spitzer proposal 11086 (PI: Mark Lacy). The National Radio Astronomy Observatory is a facility of the National Science Foundation operated under cooperative agreement by Associated Universities, Inc. This work is based on observations made with the *Spitzer Space Telescope*, which is operated by the Jet Propulsion Laboratory (JPL), California Institute of Technology (Caltech), under a contract with NASA. Numerical computations were done on the Sciama High Performance Compute (HPC) cluster which is supported by the ICG, SEPNet, and the University of Portsmouth. Data used in this paper are based on observations obtained with MegaPrime/MegaCam, a joint project of CFHT and CEA/IRFU, at the Canada-France-Hawaii Telescope (CFHT) which is operated by the National Research Council (NRC) of Canada, the Institut National des Science de l'Univers of the Centre National

de la Recherche Scientifique (CNRS) of France, and the University of Hawaii. This work is based in part on data products produced at Terapix available at the Canadian Astronomy Data Centre as part of the Canada-France-Hawaii Telescope Legacy Survey, a collaborative project of NRC and CNRS.

REFERENCES

Abolfathi B. et al., 2018, ApJS, 235, 42
Afonso J. et al., 2011, ApJ, 743, 122
Arnouts S., Cristiani S., Moscardini L., Matarrese S., Lucchin F., Fontana A., Giallongo E., 1999, MNRAS, 310, 540
Baldry I. K. et al., 2018, MNRAS, 474, 3875
Baum W. A., 1962, in McVittie G. C., ed., Proc. IAU Symp. 15, Problems of Extra-Galactic Research, Photoelectric Magnitudes and Red-Shifts. Kluwer, Dordrecht, p. 390
Benítez N., 2000, ApJ, 536, 571
Berta S. et al., 2006, A&A, 451, 881
Berta S. et al., 2008, A&A, 488, 533
Bertin E., Arnouts S., 1996, A&AS, 117, 393
Bolzonella M., Miralles J.-M., Pelló R., 2000, A&A, 363, 476
Bradshaw E. J. et al., 2013, MNRAS, 433, 194
Brammer G. B., van Dokkum P. G., Coppi P., 2008, ApJ, 686, 1503
Brammer G. B. et al., 2009, ApJ, 706, L173
Bruzual G., Charlot S., 2003, MNRAS, 344, 1000
Calzetti D., Armus L., Bohlin R. C., Kinney A. L., Koornneef J., Storchi-Bergmann T., 2000, ApJ, 533, 682
Chen C.-T. J. et al., 2018, MNRAS, 478, 2132
Childress M. J. et al., 2017, MNRAS, 472, 273
Coil A. L. et al., 2011, ApJ, 741, 8
Cool R. J. et al., 2013, ApJ, 767, 118
Cooper M. C. et al., 2012, MNRAS, 425, 2116
Dahlen T. et al., 2013, ApJ, 775, 93
Dickinson M., Giavalisco M. GOODS Team, 2003, in Bender R., Renzini A., eds, The Mass of Galaxies at Low and High Redshift The Great Observatories Origins Deep Survey. Springer-Verlag, New York,p. 324
Eales S. et al., 2009, ApJ, 707, 1779
Edge A. et al., 2013, The Messenger, 154, 32
Emerson J. P., Sutherland W. J., McPherson A. M., Craig S. C., Dalton G. B., Ward A. K., 2004, The Messenger, 117, 27
Fazio G. G. et al., 1998, in Fowler A. M., ed., Proc. SPIE Conf. Ser. Vol. 3354, Infrared Astronomical Instrumentation, Infrared array camera (IRAC) for the Space Infrared Telescope Facility (SIRTF). SPIE, Bellingham, p. 1024
Fazio G. G. et al., 2004, ApJS, 154, 10
Galametz A. et al., 2013, ApJS, 206, 10
Garilli B. et al., 2014, A&A, 562, A23
Giacconi R. et al., 2001, ApJ, 551, 624
González-Fernández C. et al., 2018, MNRAS, 474, 5459
González-Solares E. A. et al., 2011, MNRAS, 416, 927
Grogin N. A. et al., 2011, ApJS, 197, 35
Guo Y. et al., 2013, ApJS, 207, 24
Guzzo L. The Vipers Team, 2013, The Messenger, 151, 41
Gwyn S. D. J., 2012, AJ, 143, 38
Hasinger G., Burg R., Giacconi R., Hartner G., Schmidt M., Trumper J., Zamorani G., 1993, A&A, 275, 1
Hewett P. C., Warren S. J., Leggett S. K., Hodgkin S. T., 2006, MNRAS, 367, 454
Hildebrandt H. et al., 2010, A&A, 523, A31
Hoaglin D. C., Mosteller F., Tukey J. W., 1983, Understanding Robust and Exploratory Data Analysis. Wiley, New York
Hsu L.-T. et al., 2014, ApJ, 796, 60
Huber P. J., 1981, Robust Statistics. Wiley, New York
Ilbert O. et al., 2006, A&A, 457, 841
Ilbert O. et al., 2009, ApJ, 690, 1236
Ilbert O. et al., 2013, A&A, 556, A55
Jarvis M. J. et al., 2013, MNRAS, 428, 1281
Kim J.-W. et al., 2014, MNRAS, 438, 825
Koekemoer A. M. et al., 2011, ApJS, 197, 36
Lacy M.et al., 2004, ApJS, 154, 166
Lacy M., Ridgway S. E., Sajina A., Petric A. O., Gates E. L., Urrutia T., Storrie-Lombardi L. J., 2015, ApJ, 802, 102
Laidler V. G. et al., 2007, PASP, 119, 1325
Lang D., Hogg D. W., Schlegel D. J., 2016, AJ, 151, 36
Lawrence A. et al., 2007, MNRAS, 379, 1599
Le Fèvre O. et al., 2005, A&A, 439, 845
Le Fèvre O. et al., 2013, A&A, 559, A14
Le Fèvre O. et al., 2015, A&A, 576, A79
Lee S., Idzi R., Ferguson H. C., Somerville R. S., Wiklind T., Giavalisco M., 2009, ApJS, 184, 100
Liske J. et al., 2015, MNRAS, 452, 2087
Lonsdale C. J. et al., 2003, PASP, 115, 897
Luchsinger K. M. et al., 2015, AJ, 150, 87
Mao M. Y. et al., 2012, MNRAS, 426, 3334
Maraston C., 2005, MNRAS, 362, 799
Maraston C., Pforr J., Renzini A., Daddi E., Dickinson M., Cimatti A., Tonini C., 2010, MNRAS, 407, 830
Mauduit J.-C., Lacy M., Farrah e., 2012, PASP, 124, 714
McCracken H. J. et al., 2012, A&A, 544, A156
McLure R. J. et al., 2013, MNRAS, 428, 1088
McMahon R. G., Banerji M., Gonzalez E., Koposov S. E., Bejar V. J., Lodieu N. , Rebolo R., VHS Collaboration , 2013, The Messenger, 154, 35
Mitchell P. D. Lacey C. G., Baugh C. M., Cole S., 2013, MNRAS, 435, 87
Mobasher B. et al., 2015, ApJ, 808, 101
Moncelsi L. et al., 2011, ApJ, 727, 83
Nyland K. et al., 2017, ApJS, 230, 9
Oliver S. et al., 2000, MNRAS, 316, 749
Oliver S. J., 1996, in Bremer M. N., Malcolm N., eds, Astrophysics and Space Science Library, Vol. 206, Cold Gas at High Redshift, Kluwer Academic Publishers, Dordrecht, p. 77
Owen F. N., Morrison G. E., 2009, ApJS, 182, 625
Patel H., Clements D. L., Rowan-Robinson M., Vaccari M., 2011, MNRAS, 415, 1738
Pforr J., Maraston C., Tonini C., 2012, MNRAS, 422, 3285
Pforr J., Maraston C., Tonini C., 2013, MNRAS, 435, 1389
Rafelski M. et al., 2015, AJ, 150, 31
Rowan-Robinson M. et al., 2004, MNRAS, 351, 1290
Rowan-Robinson M. et al., 2008, MNRAS, 386, 697
Rowan-Robinson M., Gonzalez-Solares E., Vaccari M., Marchetti L., 2013, MNRAS, 428, 1958
Sacchi N. et al., 2009, ApJ, 703, 1778
Salim S. et al., 2007, ApJS, 173, 267
Salpeter E. E., 1955, ApJ, 121, 161
Salvato M. et al., 2009, ApJ, 690, 1250
Scodeggio M. et al., 2018, A&A, 609, A84
Scoville N. et al., 2007, ApJS, 172, 1
Simpson C. et al., 2012, MNRAS, 421, 3060
Smail I., Sharp R., Swinbank A. M., Akiyama M., Ueda Y., Foucaud S., Almaini O., Croom S., 2008, MNRAS, 389, 407,
Tasca L. A. M. et al., 2017, A&A, 600, A110
Trichas M., Georgakakis A., Rowan-Robinson M., Nandra K., Clements D., Vaccari M., 2009, MNRAS, 399, 663
Vaccari M., 2015, The Many Facets of Extragalactic Radio Surveys: Towards New Scientific Challenges The Spitzer Data Fusion: Contents, Construction and Applications to Galaxy Evolution Studies. p. 27
Vaccari M. 2016, in Astrophysics and Space Science Library, Vol. 42, The Universe of Digital Sky Surveys. Springer International Publishing, Switzerland, p. 71
Vaccari M. et al., 2005, MNRAS, 358, 397

Vaccari M. et al., 2016, Proceedings of the 4th Annual Conference on High Energy Astrophysics in Southern Africa (HEASA 2016). January 13th, 2016. South African Astronomical Observatory (SAAO), Cape Town, South Africa. Available at: http://pos.sissa.it/cgi-bin/reader/conf.cgi?confid = 275, id.26 The VOICE Survey : VST Optical Imaging of the CDFS and ES1 Fields. p. 26

Wuyts S., Franx M., Cox T. J., Hernquist L., Hopkins P. F., Robertson B. E., van Dokkum P. G., 2009, ApJ, 696, 348

Yuan F. et al., 2015, MNRAS, 452, 3047

This paper has been typeset from a TEX/LATEX file prepared by the author.